https://doi.org/10.5194/egusphere-2025-2329
Preprint. Discussion started: 11 June 2025

Snow Water Equivalent Retrieval and Analysis Over Altay Using 12-Day Repeat-Pass Sentinel-1 Interferometry

Jingtian Zhou[1,2], Yang Lei[1], Jinmei Pan[1], Cunren Liang[3], Yunjun Zhang[2,4], Weiliang Li[1,2], Chuan Xiong[5], Jiancheng Shi[1]

[1]National Space Science Center, Chinese Academy of Sciences, Beijing, 100190, China
[2]University of Chinese Academy of Sciences, Beijing, 100049, China
[3]School of Earth and Space Sciences, Peking University, Beijing, 100871, China
[4]National Key Laboratory of Microwave Imaging, Aerospace Information Research Institute, Chinese Academy of Sciences, Beijing, 100094, China
[5]Southwest Jiaotong University, Faculty of Geosciences and Engineering, Chengdu, 611756, China

Correspondence to: Yang Lei (leiyang@nssc.ac.cn)

Abstract. Accurate Snow Water Equivalent (SWE) estimation is significant for understanding global climate change, surface energy balance, and regional water cycles. However, although there have been many studies on the inversion of SWE using active and passive microwave remote sensing, it remains challenging to assess the global distribution of SWE with sufficient temporal and spatial resolution and accuracy. Interferometric Synthetic Aperture Radar (InSAR) has become a promising technique for SWE change estimation, which is limited by the optimal radar frequencies and revisit intervals that have not been available until recently. In this study, 12-day Sentinel-1 C-band InSAR data from 2019 to 2021 are used to retrieve ΔSWE (SWE changes in one InSAR pair) and cumulative SWE in the Altay region of Xinjiang, China. The correlation between the retrieved ΔSWE and in-situ observations reaches R=0.48, with a low RMSE of 15.5 mm (n=241) throughout the two whole snow seasons, improving to R=0.47 and RMSE of 15.9 mm for 2019-2020, and R=0.51 and RMSE of 14.8 mm for 2020-2021. These results are achieved without filtering for low coherence or high temperatures. Heavy snowfall leads to decorrelation and phase unwrapping errors, which affect ΔSWE retrieval and are propagated into cumulative SWE. Validation of the cumulative SWE after removing wet snow yields an RMSE of 36.5 mm, which improves to 28.4 mm when high-elevation stations with unwrapping errors due to heavy snowfall are also excluded. InSAR-derived cumulative SWE time series show consistency with ground observations at some stations, though slight overestimations and underestimations are observed due to error accumulation. Various factors combined with validation results show that higher coherence, lower air temperature, and reliable snow density improve the retrieval accuracy. The proposed phase calibration method demonstrates that selecting at least half of the available in-situ ΔSWE values for calibration yields reliable ΔSWE estimates. Calibrating only the integer multiples of 2π provides reasonable accuracy, but is still inferior to the full calibration method, indicating that residual modulo 2π phase has a noticeable contribution to the final inversion accuracy, which highlights that phase calibration plays a key role in the accurate ΔSWE retrieval. This study provides a valuable reference and processing prototype for applying 12-day revisit Sentinel-1 and future NISAR InSAR data to SWE monitoring.

https://doi.org/10.5194/egusphere-2025-2329
Preprint. Discussion started: 11 June 2025

1 Introduction

Snow significantly influences the balance of surface radiation energy due to its high albedo, thermal insulation properties, and heat absorption during melting periods (You et al., 2020). These characteristics make snow become an essential indicator of the global climate system (Aguirre et al., 2018). Snowmelt is a crucial source of water resources to billions of people worldwide (Barnett et al., 2005). Snow water equivalent (SWE) is defined as the height of liquid water would be produced if a snow column of a specified thickness area completely melts into water, and it is a crucial input parameter in hydrological processes, ecological models, and climate system models (Derksen et al., 2010), while also playing a key role in the energy transfer process between soil and atmosphere. However, evaluating the global distribution of SWE with adequate temporal and spatial resolution and accuracy remains challenging.

Passive microwave (PM) remote sensing, based on the microwave emissions from snowpack (Foster et al., 1997), is currently the main method of retrieving daily spatiotemporal information on SWE at a large scale. This method will become saturated for SWE larger than 150 mm, which limits their use in mountainous areas. Many research has been conducted using passive microwave remote sensing to estimate snow depth and SWE (Takala et al., 2011; Dai Liyun et al., 2012; Tedesco and Jeyaratnam, 2016). While satellite-based passive microwave remote sensors have provided valuable insights for global estimation of cryosphere snow depth (SD)/SWE, they have limited spatial resolution, typically at the 10-kilometer level. Although a large amount of efforts have provided accurate SWE products using PM observations, existing SWE products still do not meet the minimum accuracy requirements for hydrological applications (Brown et al., 2018).

Active microwave (radar) has shown stronger applicability in basin-scale snow research due to its high spatial resolution (tens of meters typically) and sensitivity to snow parameters (Storvold et al., 2006; Shi and Dozier, 1996; Thakur et al., 2012). This technique relies on backscattering from the volume scattering of snow. Higher frequencies (Ku and X-band) have been used to estimate SWE (Rott et al., 2010; Yueh et al., 2009; King et al., 2018; Zhu et al., 2021). However, a single parameter retrieval of SWE is challenging because radar backscatter is a function of several other parameters, including snow density, snow depth, snowpack liquid water content, snow stratigraphy, snow grain size, and soil/vegetation conditions, as well as systematic factors (frequency, polarisation). Moreover, snow microstructure parameters are hard to assess over a large scale (Rutter et al., 2019).

Recently, repeat-pass Interferometric Synthetic Aperture Radar (InSAR) offers a promising approach to obtaining SWE changes at high spatial resolution and accuracy (depending on wavelength, e.g., 15 mm at L-band, 3.75mm at C-band.) by capturing radar phase changes. The method for retrieving SWE using InSAR was first proposed by Guneriussen et al. in 2001 (Guneriussen et al., 2002). The advantage of this approach is that at low frequencies, the stratigraphy of the snow hardly affects the retrieval of SWE (Yueh et al., 2017), and knowledge of snow microstructure is not required. Subsequently, the technique is applied under various conditions, including a range of frequencies, temporal baseline pairs, and different acquisition platforms. It was applied to C-band spaceborne repeat-pass InSAR datasets from ERS with a short temporal baseline of 3-day which is conducted on the Austrian Alps (Rott et al., 2003) and the North Slope of Alaska (Deeb et al., 2011). The C-band spaceborne repeat-pass InSAR datasets from Sentinel-1 with a 6-day revisit during winter over Idaho are applied to retrieve SWE (Oveisgharan et al., 2024). The higher frequency X/Ku-band is explored using dense time series from a ground-based radar (Leinss et al., 2015). Demonstrations of low-frequency L-band are based on a variety of airborne InSAR data, such as a 4-month dataset from DLR's E-SAR (Rott et al., 2003), 12-day pairs from NASA/JPL's UAVSAR (Marshall, 2020), and 8-day temporal baselines also from UAVSAR (Hoppinen et al., 2023). Additionally, temporal baselines ranging from 5 to 20 days are analyzed from UAVSAR pairs in forested areas (Bonnell et al., 2024). Spaceborne L-band, 4-month InSAR pairs from ALOS-2 are examined over regions with sparse vegetation (Lei et al., 2023). In the Altay region of Xinjiang province, China, available historical L/C-band InSAR datasets (e.g., JAXA's ALOS, ESA's Sentinel-1, and China's Lutan-1) are utilized to produce SWE change products (Lei et al., 2024). These investigations demonstrate that low-frequency radar signals, combined with shorter revisit times, can enhance penetration and reduce temporal decorrelation. This makes them particularly suitable for monitoring SWE in areas with frequent snowfall. Nevertheless, the limited availability of satellite observations with suitable frequencies and temporal baselines cause a challenge to the widespread application of this technique.

At present, Sentinel-1 data with a 6-day revisit period and InSAR method have been used to retrieve SWE in Idaho, USA, and good results have been obtained (Oveisgharan et al., 2024). However, the use of spaceborne data and the InSAR method for SWE retrieval has not been widely examined. In most regions globally, only a 12-day revisit period of Sentinel-1 data can be achieved (Kellndorfer et al., 2022). The retrieval performance under a 12-day revisit period with C-band spaceborne data has not been well studied. In this study, we evaluated the performance of SWE retrieval over Altay using interferometry based on 12-day C-band Sentinel-1 data. In Sect. 2, we introduce the study area and dataset used. Section 3 describes the methodology we use, which shows how we processed Sentinel-1 data and transform it to SWE. Section 4 introduces the comparison between the retrieved SWE with in-situ data, followed by factors that may influence the results in Sect. 5. At last, the conclusions are provided in Sect. 6.

2 Study Area and Datasets

2.1 Study Area

Altay Prefecture (44°59′35″ ~ 49°10′45″N, 85°31′57″ ~ 91°01′15″E) of Xinjiang province is situated in the region of northwestern China, covering a total area of approximately 118,000 km^2, which borders Kazakhstan, Russia, and Mongolia. Altay Prefecture is one of the regions with rich seasonal snowmelt water resources, providing snow water resources for these four countries. The average annual snow depth is approximately 40 centimeters, with a maximum over 70 cm (Dai et al., 2022). The snow accumulation period is from October to late March or early April, which lasts about 5 to 6 months. The snow density is small, with a typical value of 0.2 g·cm^{-3} (Yue et al., 2017). The region experiences a typical temperate continental climate with shorter, warm, and rainy summers and long and severely cold winters with much snow, and with a mean annual temperature ranging from 0.7 °C to 4.9 °C (Fu et al., 2017). The terrain is low in the southwest and high in the northeast (Fig. 1). The northeastern part of Altay is mountainous, with elevations rising over 3000 m. The center area is flatter, ranging between 700-800 m. The southwest is the lowest, at around 600 m. Our core study area is located in the Altay region of Xinjiang, China, between 47.80 ° and 48.26 °N and 88.05 ° and 88.68 °E, around 50×50 km.

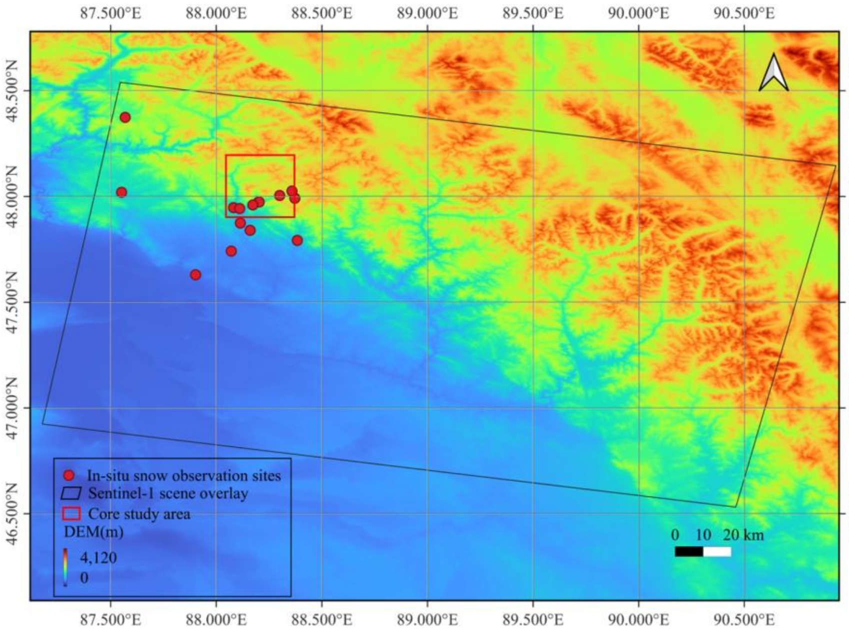

Figure 1: Location of study area, including 15 in-situ snow station points.

2.2 Datasets

2.2.1 Sentinel-1

The European Space Agency's (ESA) Copernicus Sentinel-1 mission was launched by the in 2014 with the Sentinel-1A satellite, launched on 3 April 2014, complemented with the second Sentinel-1B, launched on 25 April 2016. Each satellite has a 12-day repeat cycle. They orbit 180° apart, together imaging the Earth every 6 days but only in limited regions, which are predominantly over Europe (Kellndorfer et al., 2022). Sentinel-1 supports dual polarization and delivers products quickly. The data can be freely accessed from the Alaska SAR Facility (ASF, https://search.asf.alaska.edu/). The Sentinel-1 radar operates at C-band (5.405GHz) and offers four imaging modes. These modes vary in resolution, reaching as fine as 5 m, and cover up to 400 km. The main operational mode used in this study is the Interferometric Wide swath (IW) mode, which operates as TOPS mode, offering a large swath width of 250 km with a ground resolution of 5×20 m in range and azimuth, respectively (Torres et al., 2012). Hence, a 15×5 (range×azimuth) multilooking is applied, resulting in a final resolution of 75×100 m. For this study, Sentinel-1 Single Look Complex (SLC) data is collected over the Altay region. 19 scenes (path:19, frame:434) were acquired every 12 days from September 5, 2019, to April 8, 2020, and 18 scenes from September 11, 2020, to April 3, 2021. The data corresponds to path 19, frame 434, with a descending flight direction.

2.2.2 In-situ snow observations

The observation data of snow parameters, including snow depth and SWE, is collected from in-situ sites established by the Altay Meteorological Institute and from our own established observation stations. A total of 15 sites are available from 2019 to 2021. These sites are primarily situated in flat areas to minimize the influence of surrounding vegetation. Among these sites, only two measure SWE using snow pillow, while the remaining 13 sites measure snow depth. Snow depth sites use lasers, or snow poles and cameras. The snow depth obtained by laser is automatically obtained with a shorter interval of 10 minutes or one hour. However, the snow depth of the photographic snow observation station needs to be read manually with a slightly longer interval of 3-4 hours. The locations and environments of the snow depth measurement sites using snow poles and cameras are shown in Fig. 2. SWE data are collected less frequently, with 3 to 7 days intervals. For SWE's validation purposes, snow depth is converted to SWE using the snow density from ERA5. Observations that are closest to satellite pass times are selected for this validation.


(a) Xiaodonggou, 1241 m (b) Hongfuqiao, 1793 m (c) Wuxilike-muban, 2093 m (d) Wuxilike, 2146 m

(e) Wuzhiquan, 958 m (f) Jiayilemacun, 594 m (g) Dadonggou, 1076 m (h) Locations of (a) to (g)

Figure 2: In-situ snow depth observation sites using depth poles captured by the camera. There are several typical kinds of land cover, including valley sites: (a) Xiaodong and (g) Dachonggou, conifer forest in the shade aspect hill: (b) Hongfuqiao, plain sites:(c) Wuxilike-muban, (d) Wuxilike, (g) Jiayilemacun and (h) Wuzhiqhuan. (h) shows these sites' locations in the study area.

2.2.3 Auxiliary data

In this study, the auxiliary data are acquired for the following purposes: snow density is utilized to compute snow water equivalent (SWE) across multiple snow depth (SD) stations, air temperature data supports subsequent analyses, and digital elevation models (DEMs) along with precise orbit data are necessary for the InSAR processing of Sentinel-1 SLC data.

ERA5-Land is a reanalysis dataset (https://cds.climate.copernicus.eu/datasets/reanalysis-era5-single-levels?tab=overview) providing a consistent view of the evolution of land variables over several decades at an enhanced resolution compared to ERA5. The data are free and available through Climate Data Store. We obtain ERA5 air temperature and snow density data in our study area at the time (00:00 UTC) closest to the satellite pass (00:13 UTC). Here, the air temperature is defined as the temperature of air at 2m above the surface of the land, which is calculated by interpolating between the lowest model level and the Earth's surface, taking account of the atmospheric conditions. Temperature measured in kelvin can be converted to degrees Celsius (°C) by subtracting 273.15. The snow density we use is derived from the ECMWF Integrated Forecast System (IFS) model. This model represents snow as a single additional layer over the uppermost soil level, which may cover all or part of the grid box. The dataset has a horizontal resolution of 0.1° × 0.1° (a native resolution of 9 km) and an hourly temporal resolution. It can be predicted that the snow density has a large spatial scale (9 km), which exceeds the spatial scale of the SAR (tens of meters) we use to invert SWE. Therefore, in addition to the uncertainty in the snow density data, the spatial scale mismatch may introduce errors. For Sentinel-1 SLCs' InSAR process input data, digital elevation models (DEMs) and precise orbit data are acquired from Shuttle Radar Topography Mission (SRTM) DEM and the ASF (https://s1qc.asf.alaska.edu/aux_poeorb/), respectively.

3 Methodology

To achieve the goal of assessing the performance of 12-day Sentinel-1 C-band InSAR for monitoring SWE changes in the whole snow season, a series of components are described, including the theory of SWE retrieval from interferometric phase, data processing procedures, and the phase calibration method. In particular, Sect. 3.1 explains the theory of InSAR-derived SWE. Section 3.2 describes the workflow of stack processing Sentinel-1 SLCs to generate the interferometric phase of nearest neighbour dates, then processing of InSAR phases to produce a time series phase changes after correction of atmospheric delay and DEM error, and finally converting the phase change to SWE change. Section 3.3 introduces the in-situ SWE processing method. Section 3.4 provides the phase calibration method for InSAR-derived SWE change by using in-situ measurements for calibration.

3.1 Relationship between ΔSWE and $\Delta\phi$

The InSAR SWE retrieval algorithm considers that the signal penetration through the snow layer to the ground and the main contribution of backscattering at the ground covered by dry snow is coming from the snow-ground interface, and the volume scattering effect on the interferometric can be neglectable confirmed by the ground-based experiment (Matzler, 1996). The

https://doi.org/10.5194/egusphere-2025-2329
Preprint. Discussion started: 11 June 2025

complex permittivity properties of snow, which are strongly dependent on the liquid water content, govern the propagation of radar waves in snow. At C-band, dry snow has a typical penetration depth of 20 m (Matzler, 1996; Rott et al., 2003), while wet snow with liquid water content is limited to a few centimeters due to a prominent rise in imaginary part of permittivity as water content increases.

The real parts of the complex permittivity ε_s is a function of snow density as shown in Eq. (1) (Matzler, 1996):

$$\varepsilon_s = 1 + 1.60\rho_s + 1.86{\rho_s}^3 \tag{1}$$

where ρ_s is specified in g/cm^3.

Because snow has a different dielectric constant from air, radar waves undergo refraction as they propagate through a snow layer. When comparing the optical path lengths of radar waves without and with snow conditions, a path delay can be observed. The delay arises from the change in optical path length, given by $n \cdot s$ (where n is the refractive index and s is the geometric path length), caused by refraction within the snowpack and the reduced propagation velocity of radar waves in snow compared to air. The signal delay can be derived from the geometry path illustrated in Fig. 3. Furthermore, this path delay also occurs when there is a change in snow depth ΔZ_s, between two measurements, with the delay being proportional to ΔZ_s. This delay in path length induces a differential interferometric synthetic aperture radar (DInSAR) phase difference, which can be correlated with the change in snow depth.

By analyzing the geometric configuration presented in Fig. 3, the relationship between changes in ΔSWE and the differential interferometric phase shift observed between two SAR acquisitions $\Delta\phi$ can be written as (Guneriussen et al., 2002)

$$\Delta\phi = 2k_i \cdot \Delta Z_s \left(\cos\theta - \sqrt{\varepsilon_s - sin^2\theta}\right) \tag{2}$$

Leinss et al. derives a nearly linear dependence between ΔSWE and $\Delta\phi$ by approximating the snow density dependent permittivity term from (1) into (2) using a Taylor expansion under low density and small incidence angle assumptions, leading to the simplified expression in (3) (Leinss et al., 2015):

$$\Delta\phi = 2k_i \cdot \frac{\alpha}{2}\left(1.59 + \theta^{\frac{5}{2}}\right) \cdot \Delta SWE \tag{3}$$

where $\Delta\phi$ is the interferometric phase, ΔSWE is the change of the SWE, and the wavenumber is defined by $k_i = \frac{2\pi}{\lambda}$ with λ being the central wavelength of the radar. The incidence angle at the air-snow interface is given by θ. The optimal α is close to 1 for common incidence angles ($< 50°$). $\Delta\phi$ can be estimated from unwrapped InSAR phase. We utilize Eq. (3) to retrieve SWE, with the parameter α set to 1 in this study.

The main advantage of this method is its simplicity and does not need prior knowledge, while the main limitation is the problem of the phase unwrapping when the SWE change is larger than typically 1-2 wavelengths. Still, the wet snow absorption during the snow melt and when large snowfalls occur will limit the ability of this method (Storvold et al., 2006). This method is designed for dry snow conditions.

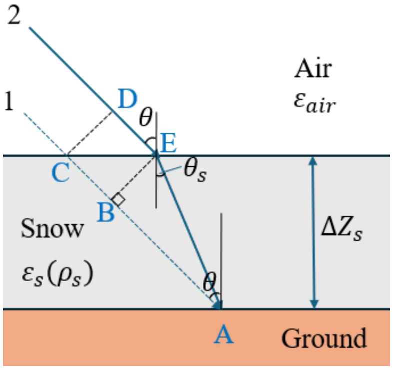

Figure 3: Propagation path of radar wave through atmosphere with snow-free and snow-covered ground for a fixed pixel. For conditions without snow, the radar wave travels the distance CA, while for snow-covered conditions, the distance is DE+EA. θ is the incidence angle, θ_s is the refracted angle in snow, ε_s is the real part of the permittivity of the snow, ε_{air} is the real part of the permittivity of the air, and ΔZ_s is the increase in snow depth between the snow-free and snow-covered ground images.

3.2 Sentinel-1 interferometric phase processing methods and procedures

The InSAR stack processing is performed using the NASA/JPL's open-source software ISCE2 (https://github.com/isce-framework/isce2) along with the time series tool MintPy (https://github.com/insarlab/MintPy). As shown in Fig. 4, the workflow consists of three main blocks: (i) InSAR stack processing for Sentinel-1 TOPS data using ISCE (Fattahi et al., 2016), (ii) InSAR time series analysis from a stack of unwrapped interferograms to phase time-series using MintPy (Yunjun et al., 2019), and (iii) phase calibration and SWE inversion.

In the first stage, after the co-registration, filtering, and phase unwrapping procedures, stacks of all secondary single-look complex (SLC) images are co-registered to the reference SLC. A coregistered stack of SLCs are produced, and the burst interferograms are merged. Merged interferograms are multilooked, filtered and unwrapped. A multi-look averaging of 15×5 (range×azimuth, similar to the following) is applied to 37 SLC data scenes, resulting in a ground resolution of 75×75 m. The SNAPHU algorithm is chosen for phase unwrapping in ISCE2.

In the second stage, the outputs from the first stage are processed to generate a corrected phase time series, which is then geocoded. Errors in phase unwrapping, tropospheric delays, and topographic residuals are corrected. The tropospheric delay correction uses the PyAPS method (https://github.com/insarlab/PyAPS), which estimates differential phase delay maps based on ECMWF's ERA-5 data. To prevent the removal of long-term trends that may impact SWE inversion, the deramp step in MintPy is not used in our study.

In the third stage, the phase time series is calibrated using in-situ ΔSWE measurements. After calibration, the corrected phase measurements are used to derive ΔSWE. The details of the phase calibration method are provided in Sect. 3.3.

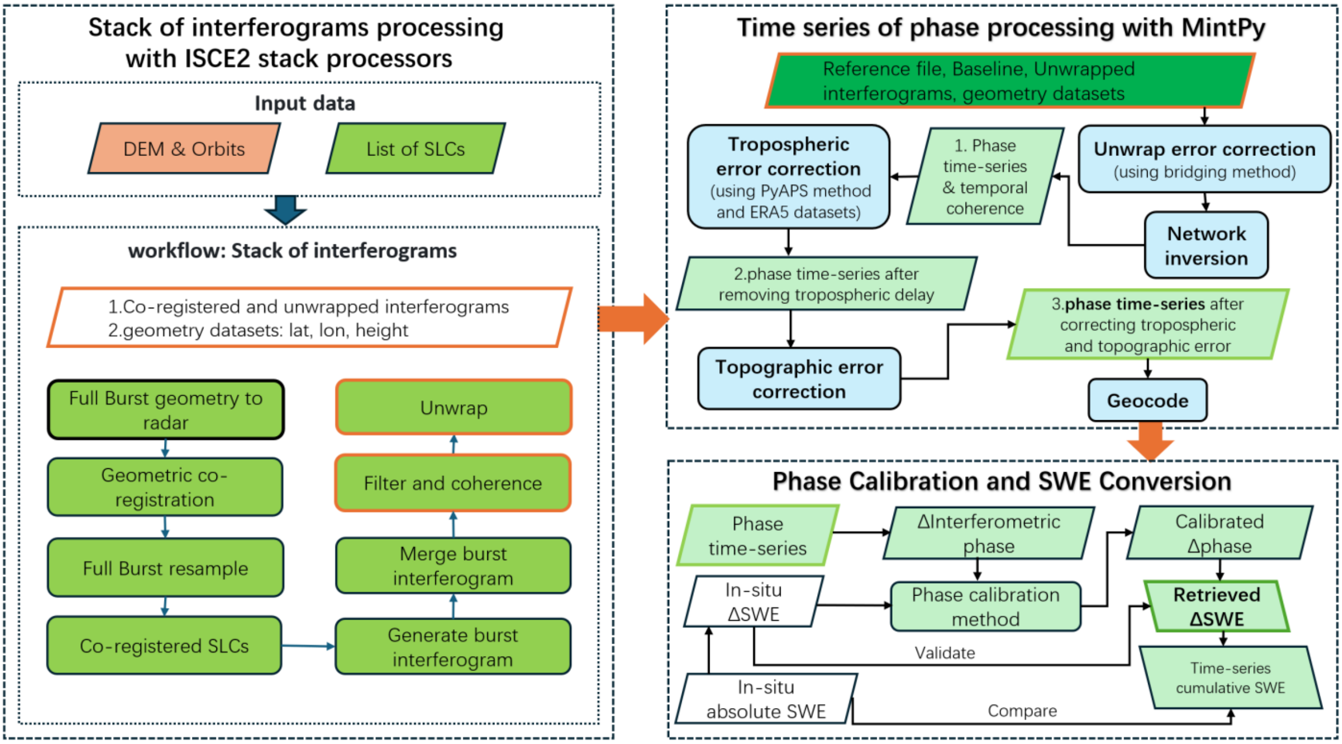

Figure 4: Flow chart of the time series InSAR Processing procedures.

3.3 In-situ SWE processing method

In-situ snow ground observations consist of measurements of snow depth and snow water equivalent (SWE).

To ensure spatiotemporal consistency with satellite overpasses, snow depth data recorded closest to the satellite observation time are selected. When minor gaps exist in the snow depth time series on the required dates, missing values are filled by averaging observations from adjacent available dates. Subsequently, snow density from the ERA5-Land dataset corresponding to the same location and time is extracted. SWE is then estimated by multiplying the snow depth by the corresponding ERA5-Land snow density.

For SWE data obtained from snow pillow observations, which are generally reliable but recorded every few days, daily interpolation is required. A direct average from adjacent days cannot be applied due to the relatively long observation intervals. Therefore, daily ERA5-Land SWE data closest to the satellite observation time are used as a reference. A least squares fitting method is applied to determine a scaling factor that brings the ERA5 SWE values closer to the in-situ observations. The scaled ERA5 SWE data are then used to interpolate the in-situ SWE observations through a fifth-order polynomial fitting. This approach enables the construction of a continuous daily SWE time series, ensuring a daily dataset aligned with the satellite's 12-day revisit cycle.

3.4 Phase calibration based on in-situ SWE

InSAR phase measurements are relative and must be calibrated to a reference point. This reference point is essential for correcting the unwrapped interferometric phase or ΔSWE in an interferometric pair. In geographical applications of InSAR, the reference point is typically chosen such that the displacement remains unchanged or is known between the two image acquisitions. For ΔSWE retrieval using InSAR, the reference point can be selected using corner reflectors with snow always being cleaned, which offer a stable zero-phase (Nagler et al., 2022; Dagurov et al., 2020), or by taking the average of in situ ΔSWE measurements (Oveisgharan et al., 2024).

However, identifying a fixed phase reference point becomes challenging, since the entire interferometric pair experiences phase changes due to snow accumulation and ablation and using a corner reflector is also labor intensive. To address this issue, the phase change at the reference point is assumed to be equivalent to the phase change in the whole scene image, which can be estimated using all available in situ SWE observations. There are several factors contributing to phase bias: integer multiple of 2π, data processing (focusing, range gating), DEM residual error, unwrapping error, atmospheric (troposphere and ionosphere) phase delay, systematic phase calibration error, etc.

3.4.1 Phase calibration method

In this study, the ground measured in-situ SWE data are used to calibrate the $\Delta\phi$, rather than calibrating the ΔSWE (Oveisgharan et al., 2024). The calibrated InSAR phase is then applied in the ΔSWE retrieval process. The interferometric phase is a direct InSAR observation, while ΔSWE is indirectly derived through modeling and approximations (e.g. dependent on local incidence angle). Calibrating the phase avoids these derivation uncertainties and accounts for incidence angle effects. This improves the reliability of SWE estimates. For this situation, the phase calibration equations can be rewritten from Eq. (3) as following:

$$\Delta\phi - C = 2k_i \cdot \frac{\alpha}{2}\left(1.59 + \theta^{\frac{5}{2}}\right) \cdot \Delta SWE \tag{4}$$

where C is the phase calibration constant for each interferogram. This C includes integer multiple of 2π and residual phase as mentioned in Sect. 3.4, which is ambiguous in phase wrapping.

Assuming we have N $(N \geq 1)$ number of interferometric pairs, so N number of C need to be estimated. Each interferometric pair has several m_n number of in-situ SWE observations for the n-th (n=1, 2, …, N) interferometric pair. We set $\boldsymbol{y} = 2k_i \cdot \frac{\alpha}{2}\left(1.59 + \theta^{\frac{5}{2}}\right) \cdot \Delta SWE$. Let $\boldsymbol{\Delta\phi}_{\boldsymbol{m_n}}$ denote the InSAR phase vector of the n-th interferometric pair, represented as the m_n by 1 vector. Similarly, let $\boldsymbol{y}_{\boldsymbol{m_n}}$ is the in-situ SWE observations vector, which is the m_n by 1 vector for the same interferometric pair. Bold represent vector (lower case) and matrix (capitalization). Then, we can get the following Eq. (5-11).

$$\boldsymbol{y} = \boldsymbol{AC} + \boldsymbol{\Delta\phi} \tag{5}$$

https://doi.org/10.5194/egusphere-2025-2329
Preprint. Discussion started: 11 June 2025

$$m = \sum_{i=1}^{N} m_i \tag{6}$$

$$\boldsymbol{y} = (\boldsymbol{y_{m_1}} \quad \boldsymbol{y_{m_2}} \quad \cdots \quad \boldsymbol{y_{m_n}})^T{}_{m\times 1} \tag{7}$$

$$\boldsymbol{v_{m_n}} = (-1 \quad \ldots \quad -1)^T{}_{m_n\times 1} \tag{8}$$

$$\boldsymbol{A} = \begin{pmatrix} \boldsymbol{v_{m_1}} & 0 & \ldots & \ldots & 0 \\ 0 & \boldsymbol{v_{m_2}} & 0 & \ldots & \vdots \\ \vdots & 0 & \boldsymbol{v_{m_3}} & \ldots & \vdots \\ \vdots & \vdots & \vdots & \ddots & 0 \\ 0 & \ldots & \ldots & 0 & \boldsymbol{v_{m_n}} \end{pmatrix}_{m\times N} \tag{9}$$

$$\boldsymbol{C} = (C_1 \quad C_2 \quad \ldots \quad C_N)^T{}_{N\times 1} \tag{10}$$

$$\Delta\boldsymbol{\phi} = (\Delta\boldsymbol{\phi_{m_1}} \quad \Delta\boldsymbol{\phi_{m_2}} \quad \cdots \quad \Delta\boldsymbol{\phi_{m_n}})^T{}_{m\times 1} \tag{11}$$

We use the least squares method to calculate C. For the $\boldsymbol{y} = A\boldsymbol{C} + \Delta\boldsymbol{\phi}$, the estimated $\widehat{\boldsymbol{C}}$ can be calculated by least squares solution as (12):

$$\widehat{\boldsymbol{C}} = (\boldsymbol{A}^T\boldsymbol{A})^{-1}\boldsymbol{A}^T(\boldsymbol{y} - \boldsymbol{\phi}) \tag{12}$$

Each interferometric phase image is calibrated based on its estimated $\widehat{C_n}$ ($n = 1,2,3 \ldots, N$). The least squares method provides an unbiased estimate of C. Specially, when only nearest InSAR pairs are considered, $\boldsymbol{A}$ is a diagonal matrix with $\boldsymbol{v_{m_n}}$ blocks that are being independent; thus, the solutions to each $\widehat{C_n}$ can be derived separately. In this scenario, for the n-th InSAR pair, the estimated $\widehat{C_n}$ represents the average value of all calibration parameters at different locations:

$$\widehat{C_n} = \left({\boldsymbol{v_{m_n}}}^T\boldsymbol{v_{m_n}}\right)^{-1}{\boldsymbol{v_{m_n}}}^T\left(\boldsymbol{y_{m_n}} - \Delta\boldsymbol{\phi_{m_n}}\right) = \frac{1}{m_n}(-1 \quad \ldots \quad -1)^T{}_{m_n\times 1}\left(\boldsymbol{y_{m_n}} - \Delta\boldsymbol{\phi_{m_n}}\right) = \frac{1}{m_n}\sum_{k=1}^{k=m_n}(\Delta\boldsymbol{\phi_k} - \boldsymbol{y}_k) \tag{13}$$

Only the nearest InSAR pair is considered because the temporal baseline in our study is already 12 days, which is relatively long compared to the rate of snow variation. Using longer baselines, such as 24 or 48 days, is less beneficial for phase unwrapping. However, if shorter temporal baseline data become available in the future, redundant interferometric pairs should be considered to estimated C, where we can not calculate $\widehat{C_n}$ from Eq. (13). Instead, we must employ the least squares method from Eq. (12) to obtain a solution where matrix $\boldsymbol{A}$ is no longer diagonal.

For example, if there are n SAR acquisitions, then $n - 1$ adjacent interference pairs can be formed. Considering all interferometric pairs, the total number of interference pairs is $\binom{2}{n} = \frac{n(n-1)}{2}$. In the case of three scenes (1st, 2nd and 3rd), there are three combinations of interferometric pairs, and theoretically C_{13}=C_{12}+C_{23}, where C_{ij} represents the calibration parameter between the i-th and j-th SAR acquisitions. The corresponding relationship among these interferometric pairs in the above three-scene case can be formulated explicitly, as shown in Eqs. (14) to (19). In this case, $\Delta\boldsymbol{\phi_{ij}}$ is the InSAR phase vector for the interferometric pair between the i-th and j-th SAR scenes, represented as the $m_{ij} \times 1$ vector corresponding to the m_{ij}

number of in-situ SWE observations. Similarly, $\boldsymbol{y_{ij}}$ represents the in-situ SWE observations vector, which is the $m_n \times 1$ vector for the same interferometric pair.

$$\boldsymbol{y} = \boldsymbol{AC} + \boldsymbol{\Delta\phi} \tag{14}$$

$$M = m_{12} + m_{23} + m_{13} \tag{15}$$

$$\boldsymbol{y} = (\boldsymbol{y_{12}} \quad \boldsymbol{y_{23}} \quad \boldsymbol{y_{13}})^T{}_{M\times 1} \tag{16}$$

$$\boldsymbol{v_{ij}} = (-1 \quad \dots \quad -1)^T{}_{m_{ij}\times 1} \tag{17}$$

$$\boldsymbol{A} = \begin{pmatrix} \boldsymbol{v_{12}} & 0 & 0 \\ 0 & \boldsymbol{v_{23}} & 0 \\ 0 & 0 & \boldsymbol{v_{13}} \end{pmatrix}_{M\times 3} \tag{18}$$

$$\boldsymbol{C} = (C_{12} \quad C_{23} \quad C_{13})^T{}_{3\times 1}$$

$$\Delta\boldsymbol{\phi} = (\Delta\boldsymbol{\phi}_{12} \quad \Delta\boldsymbol{\phi}_{13} \quad \Delta\boldsymbol{\phi}_{13})^T{}_{M\times 1} \tag{19}$$

Substituting Eqs. (15-19) into (14), we obtain (20).

$$\begin{pmatrix} \boldsymbol{y_{12}} \\ \boldsymbol{y_{23}} \\ \boldsymbol{y_{13}} \end{pmatrix}_{M\times 1} = \begin{pmatrix} \boldsymbol{v_{12}} & 0 & 0 \\ 0 & \boldsymbol{v_{23}} & 0 \\ 0 & 0 & \boldsymbol{v_{13}} \end{pmatrix}_{M\times 3} \begin{pmatrix} C_{12} \\ C_{23} \\ C_{13} \end{pmatrix}_{3\times 1} + \begin{pmatrix} \Delta\boldsymbol{\phi}_{12} \\ \Delta\boldsymbol{\phi}_{23} \\ \Delta\boldsymbol{\phi}_{13} \end{pmatrix}_{M\times 1} \tag{20}$$

Since C is a systematic calibration parameter, it follows that $C_{13} = C_{12} + C_{23}$. Therefore, Eq. (20) can be rewritten in the following:

$$\begin{pmatrix} \boldsymbol{y_{12}} \\ \boldsymbol{y_{23}} \\ \boldsymbol{y_{13}} \end{pmatrix}_{M\times 1} = \begin{pmatrix} \boldsymbol{v_{12}} & 0 \\ 0 & \boldsymbol{v_{23}} \\ \boldsymbol{v_{12}} & \boldsymbol{v_{23}} \end{pmatrix}_{M\times 2} \begin{pmatrix} C_{12} \\ C_{23} \end{pmatrix}_{2\times 1} + \begin{pmatrix} \Delta\boldsymbol{\phi}_{12} \\ \Delta\boldsymbol{\phi}_{23} \\ \Delta\boldsymbol{\phi}_{13} \end{pmatrix}_{M\times 1} \tag{21}$$

When the redundant interferometric pair C_{13} is considered, the number of equations to solve C increases, i.e., the elements in the non-diagonal area of the above $\boldsymbol{A}$ matrix will have non-0 values.

3.4.2 Phase calibration based on different numbers of selected points

To validate our phase calibration method (in Sect. 3.4.1) and test the validation accuracy under different conditions, we adopt a phase calibration method based on different numbers of selected points. According to each interferometer pair's actual in-situ ΔSWE data, only a portion of ΔSWE data is selected as calibration points, which means they are used to calculate the calibration parameters, while the other ΔSWE data are used for validation only. Because the total number of stations that can be used for calibration is small (in our case, the maximum is 13), the point selection criteria is not based on the properties corresponding to the data (such as coherence, elevation, etc.), but Monte Carlo random selection of in-situ ΔSWE data multiple times (100) is adopted.

3.4.3 Partial phase calibration for the integer multiples of 2π

The calibration parameter (C) is considered to consist of two components: the integer multiple of 2π and the residual part less than 2π. Three cases are tested to investigate the influence of different components of the calibration parameter on the ΔSWE retrieval: no phase calibration, calibration using only the integer multiple of 2π, and calibration using the full parameter. The second strategy means that only the integer multiple of 2π within the calibration parameter is used, i.e., full calibration parameter subtracts its modulo 2π. Specifically, if C is with $(-\pi, \pi)$, $C = 0$; if $C \leq -\pi$, it is replaced by -2π; if $C \geq \pi$, it is replaced by 2π. This approach removes the integer phase while ignoring the residual phase.

4 Results

This section shows the unwrapped phase and coherence of each InSAR pair in two snow seasons firstly. Then the retrieved time series scene-wide cumulative SWE is described, followed by the validation results, which compare retrieved and in-situ ΔSWE, and then assess the impact of using different numbers of calibrated points on validation accuracy. Finally, the validation of cumulative SWE and the comparison between the in-situ and retrieved time series cumulative SWE at each station is shown.

4.1 Intermediate results of InSAR processing

During the InSAR processing (Section 3.2), some intermediate results are obtained, including the unwrapped phase and coherence of each InSAR pair in two snow seasons, as shown in Figs. 5 and 6. During the snow season, some InSAR pairs show relatively high coherence, corresponding to the subfigures 7 to 10 in Fig. 5, and 6 to 11 in Fig. 6. These relatively good interference pairs will be mentioned in the subsequent validation of results in Fig. 11. The areas with higher coherence correspond to places with more robust and accurate unwrapped phases. Lower coherence corresponds to more discontinuities in unwrapped phase distributions, and more isolated areas appear in the connected component graph. These areas may increase the errors in the inversion results and result in adverse effects.

Based on the SWE and air temperature time series changes observed at the in-situ sites (see Fig. 7), several patterns can be identified for the snow season. As shown in Fig 7(a), a snowfall event was recorded in September 2019, but the corresponding interference pair dates (subplot 0 of Fig. 5) correspond to a period before and after the snowfall, resulting in little impact on the interference pair by snowfall and snowmelt. Then, up until mid-October, no snowfall is observed. During this time, changes in phase and coherence are likely caused by atmospheric variations driven by gradually decreasing temperatures, as indicated in subplots 1 and 2 of Fig. 5, in which decorrelation and obvious changes in the unwrap phase begin to occur. Snowfall starts in mid-October, leading to a continuous increase in SWE. This results in a large area of low coherence, primarily due to the impact of snowfall, as shown in subplot 3 of Fig. 5. In early November, temperatures rise above 0 °C, leading to a snowmelt process. This causes coherence to remain low, as illustrated in subplot 4 of Fig. 5. A similar low coherence remains in subplots 5 and 6 of Fig. 5, this is likely due to heavy snowfall events and temperature fluctuations around 0 °C, causing an unstable

https://doi.org/10.5194/egusphere-2025-2329
Preprint. Discussion started: 11 June 2025

snowpack state. The snowpack becomes more stable later in the snow season, accompanied by consistently low temperatures, mainly around -10 °C. During this period, coherence is high, as shown in subplots 7 to 12 of Fig. 5. After mid-February of the following year, rising temperatures lead to a snowmelt process. The presence of wet snow significantly reduces coherence, as illustrated in subplots 13 to 17 of Fig. 5.

We make a note here that, large snowfall events can cause temporal decorrelation, leading to phase unwrapping errors. Under this condition, the SWE retrieval method is not recommended. For example, as shown in Fig. 7(a), the cumulative SWE increases by about 100 mm from 4 Nov 2019 to 28 Nov 2019 over one of the high-elevation stations, which exceeds the SWE changes detection limit (approximately 30 mm for C-band, corresponding to a 2π phase change). This suggests that phase ambiguity may occur. During this period, low coherence is shown by dark areas in subplots 5 and 6 of Fig. 5, which likely leads to unwrapping errors. These errors are visible as isolated unwrapped phase patches.

The following year, a similar pattern is observed (Fig. 7(b)). The coherence is low from mid-to-late September to late November due to the snowfall and the air temperature which is not continuously below 0 °C. Lower coherence corresponds to larger unwrap phase changes. High coherence is recorded during low temperatures and stable SWE, as shown in subplots 6 to 11 of Fig. 6. In contrast, coherence decreases during the final snowmelt period when temperatures rise, as shown in subplots 12 to 16 of Fig. 6. Moreover, the coherence pattern may reveal human activities. The black line on the coherence map in September may be caused by human grazing activities. The road's coherence will recover after a period of snowfall, which may be related to the artificial snow removal in the city.

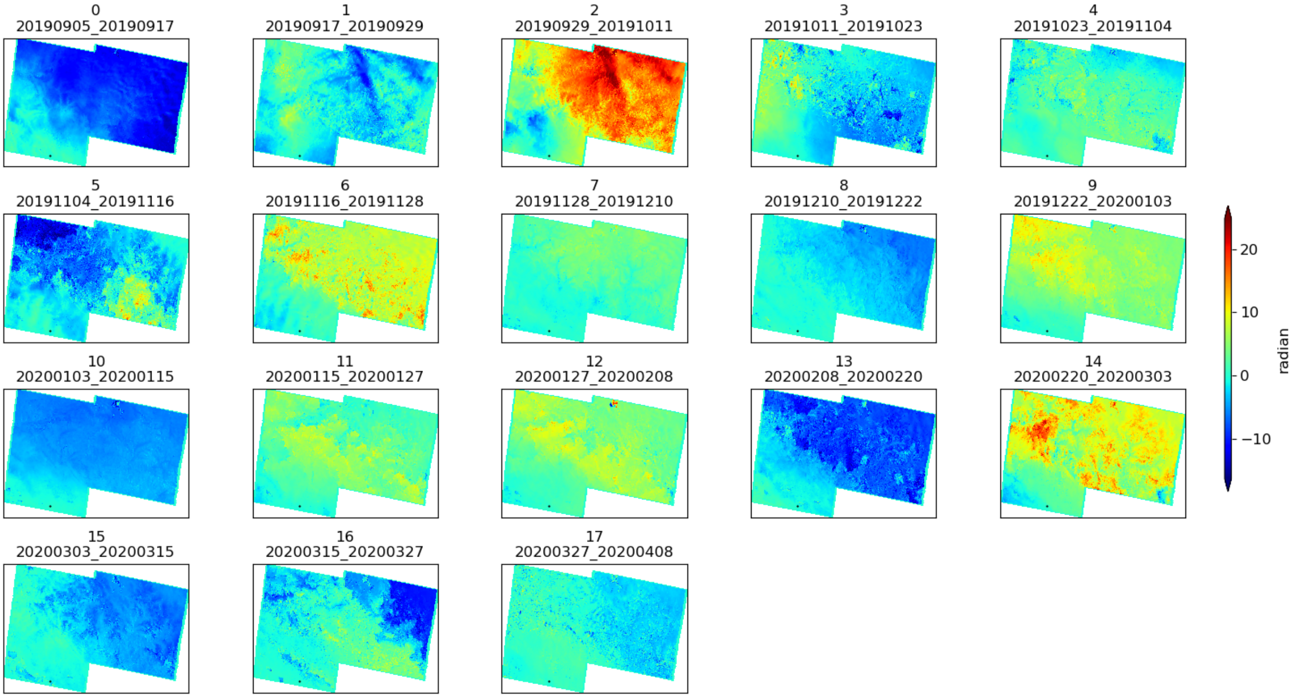

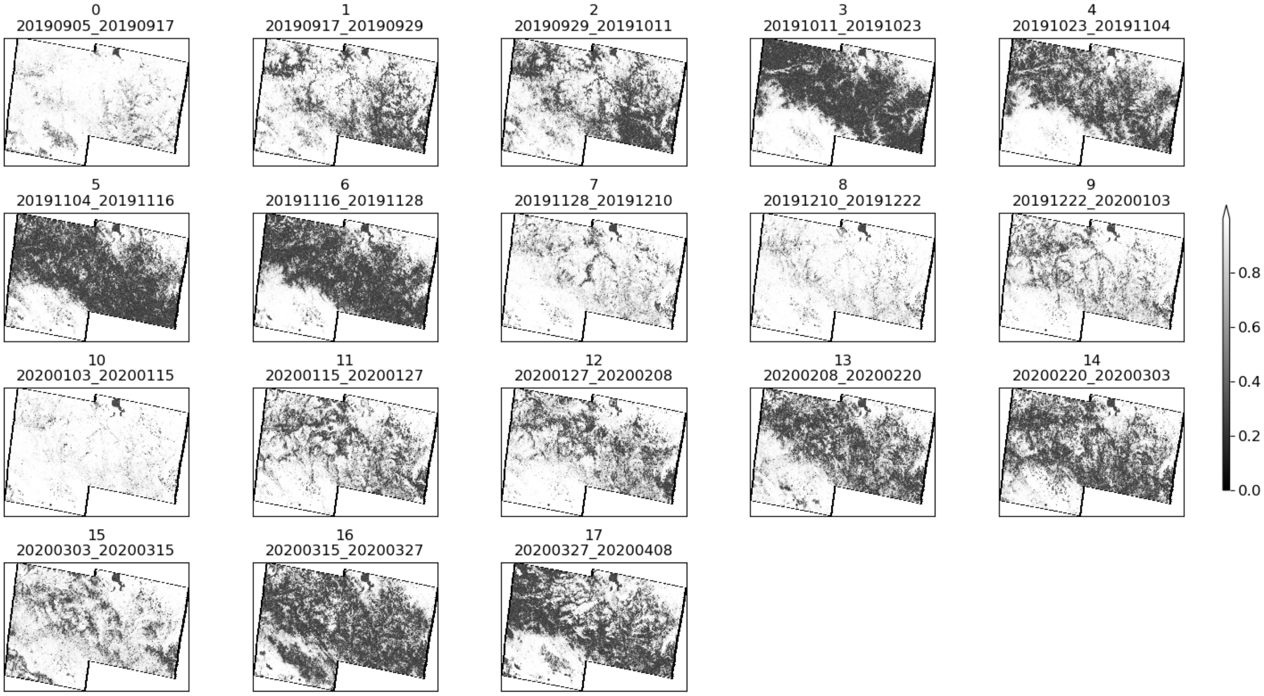

345

Figure 5: The unwrapped phase (top panel) and coherence (bottom panel) data from September 5, 2019 to April 9, 2020, every 12 days.

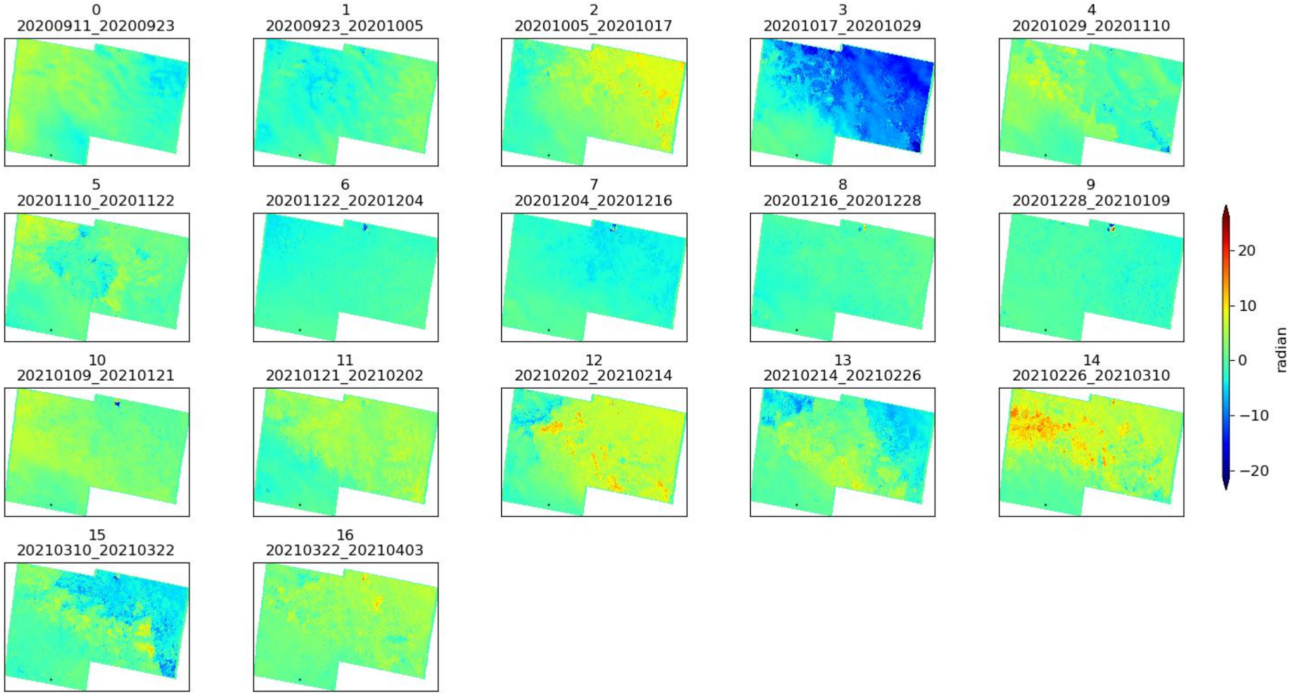

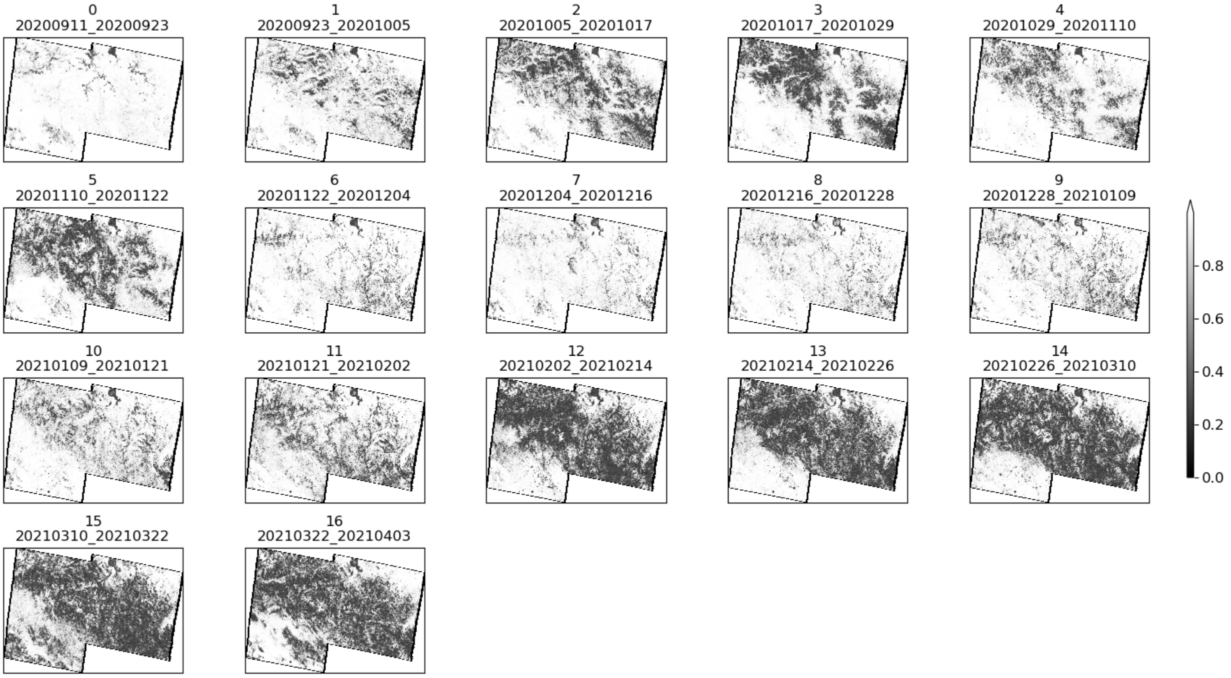

Figure 6: The unwrapped phase (top panel) and coherence (bottom panel) data from September 11, 2020 to April 3, 2021, every 12 days.

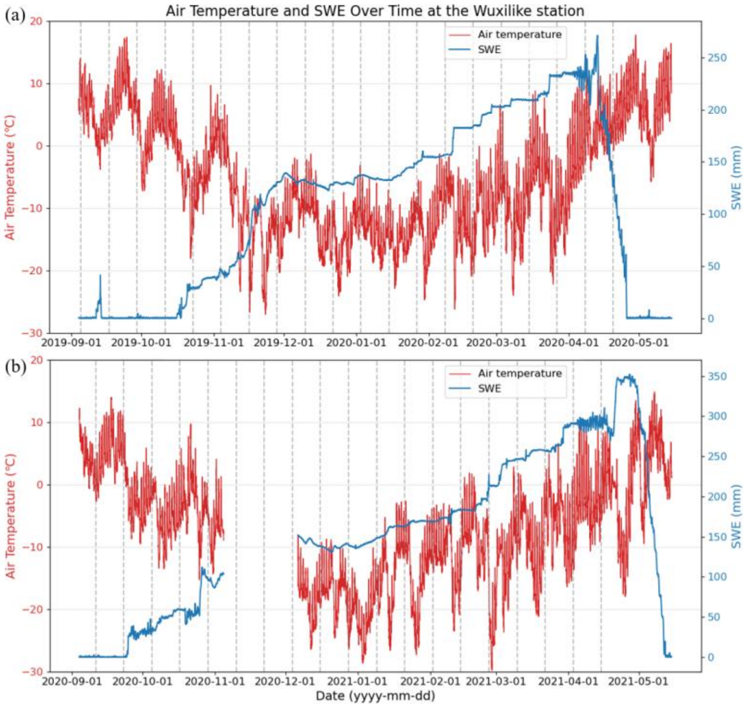

Figure 7: Observed time series in-situ SWE and air temperature change at the Wuxilike station from (a) 2019 to 2020 and (b) 2020 to 2021. (The vertical black dashed lines correspond to satellite observation dates.)

4.2 Spatiotemporal distribution/variations in cumulative SWE

Large spatial-scale cumulative SWE changes in the two snow seasons at the Altay, every 12 days, at a 75×75m spatial resolution, are mapped using InSAR and Sentinel-1 following the above InSAR processing (see Figs. 8 and 9). A comparison of Figs. 8 and 9 shows that the processes of spatial variation for accumulated SWE in both the 2019-2020 and 2020-2021 seasons are similar. In both seasons, the SWE shows a gradual increase from September to mid-March, peaking in March, followed by a decrease in the same regions from late March to early April. However, differences are also observed. In the second year, the spatial extent of maximum SWE cumulation was smaller than in the first year. Additionally, the location and the range of the region where SWE reached its peak is different between the two years.

During the 2019–2020 snow season, SWE cumulation is in a moderate pattern in the early months, from September to November, SWE increases from 0 mm to approximately 50 mm. As the season gets into the late January, significant cumulation is observed in areas A and B, located at higher elevations, while the lower-elevation area C in the southwest shows a relatively smaller increase. By mid-March, SWE reaches its maximum spatial extent, with the most notable cumulations still emerging in the higher elevations, areas A and B. A rapid decline follows in late March and early April, especially in region D, where the SWE declines significantly from approximately 120 mm on March 15 to around 25 mm.

A similar temporal process of SWE cumulation can be found in the 2020-2021 season, though with differences in the spatial variations. Early cumulation trends are as well as those of the previous year, with SWE rising to approximately 50 mm by late November. However, uneven increases appear across the study area from December to February, which may be explained in the influence of meteorological conditions and topographic factors. The most significant rise in SWE is concentrated in area A, where the peak cumulation in spatial extent is reached on March 10, 2021. A rapid SWE decrease in late March is observed in area B, which corresponds to the same location as area D from the previous season, where SWE declines from approximately 100 mm to around 50 mm. These temporal and spatial differences reflect the uneven distribution or rate of change of snow accumulation and melting processes, which is influenced by various factors during the snow season, such as differing snowfall patterns, topography, and meteorological conditions.

https://doi.org/10.5194/egusphere-2025-2329
Preprint. Discussion started: 11 June 2025

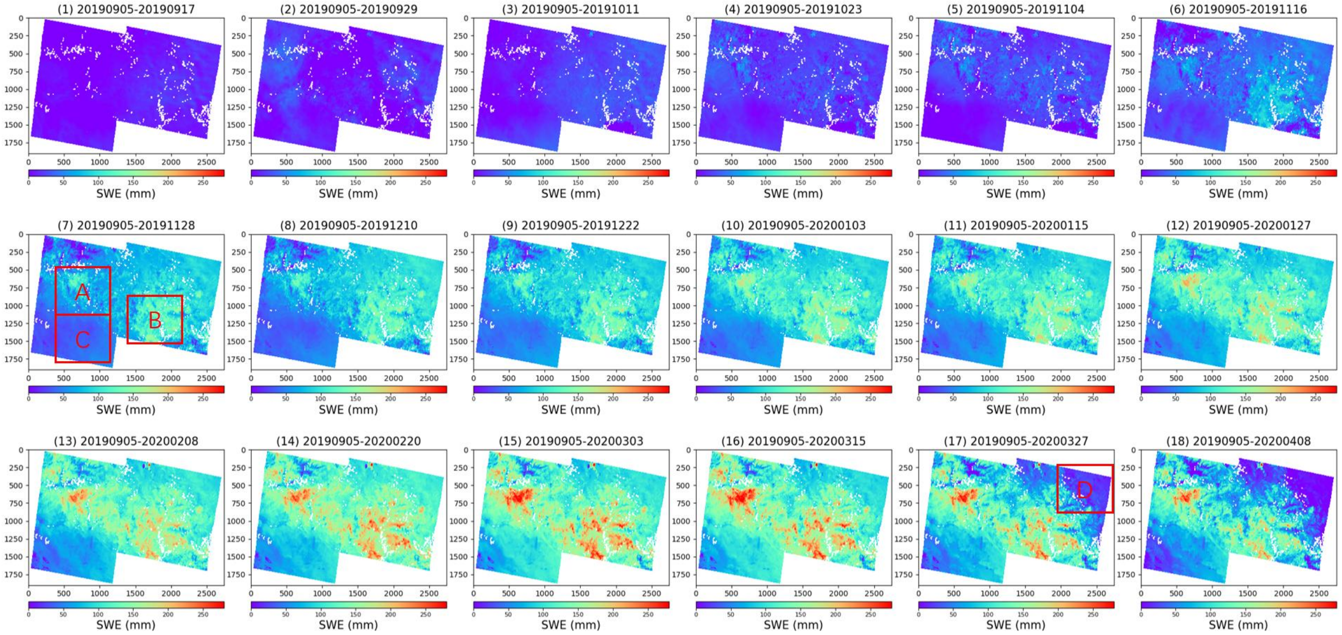

Figure 8: Spatiotemporal distribution of cumulative SWE in Altay during the 2019–2020 snow season. (Both this figure and the following one show the SWE variation relative to the first reference scene, with a 12-day cumulation interval. The geographical extent of this figure is around 182km×107km in width and height, respectively. The SWE of the reference scene is set to 0. The reference scene for this figure is September 5, 2019. The cumulation starts and end dates are shown at the top of each sub-figure. The red rectangles mark areas A, B, C, and D to describe the SWE variations across different regions. To improve comparison, these are colored in the same range)

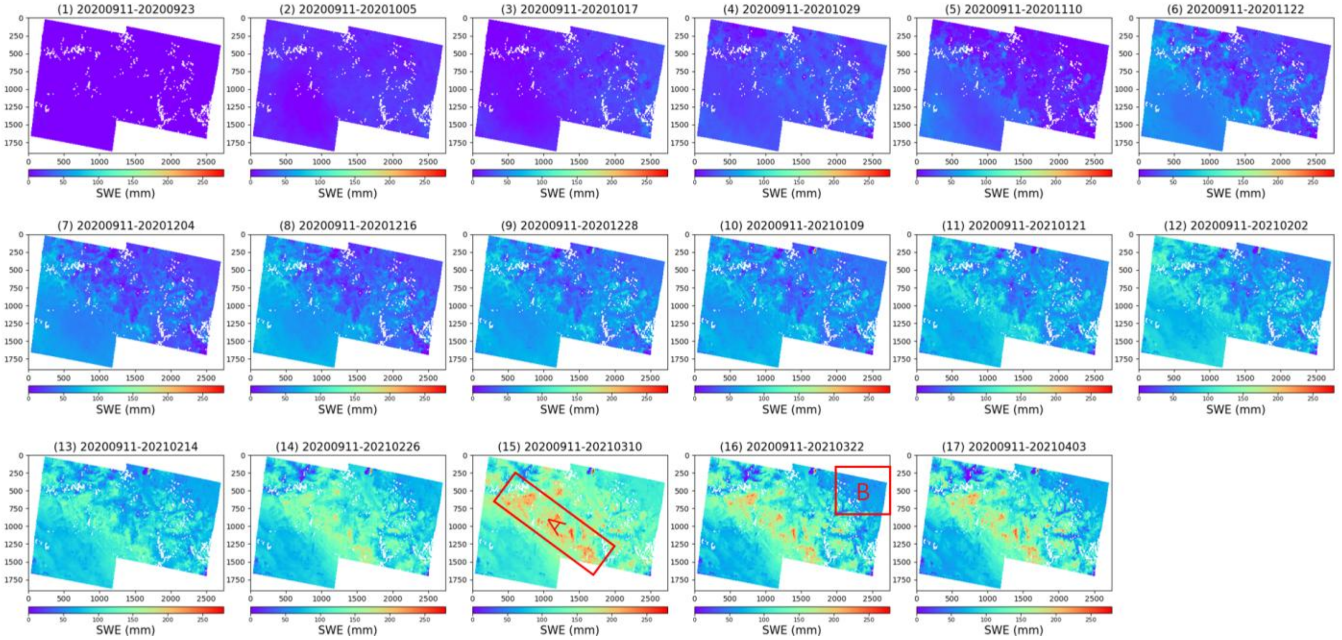

Figure 9: Spatiotemporal distribution of cumulative SWE in Altay during the 2020–2021 snow season. (The reference scene for this figure is September 5, 2020.)

https://doi.org/10.5194/egusphere-2025-2329
Preprint. Discussion started: 11 June 2025

4.3 Validation of the retrieved SWE

4.3.1 Comparing Sentinel-1 retrieved ΔSWE with in-situ ΔSWE

As shown in Fig. 10, the retrieved ΔSWE, with a 12-day temporal baseline from September 5, 2019, to April 8, 2020, and September 11, 2020, to April 3, 2021, are validated against with all in situ SWE observations, with an RMSE of 15.5 mm (R=0.48, p-value<<0.05). Here, we use a 5×5 pixel averaging on retrieved ΔSWE, corresponding to a spatial resolution of 375×375 m. The high coherence points (red) are closer to the 1:1 line with higher accuracy, while the lower coherence ones (purple) are affected by the decorrelation error sources and thus more scattered away from 1:1 line. These results prove that InSAR-derived SWE using Sentinel-1 with a 12-day revisit time is able to estimate the SWE at Altay, indicating that the importance of higher coherence is one of the key factors to obtain good retrieval results. The validation results show minor differences depending on the choice of multi-pixel averaging for the retrieved SWE.

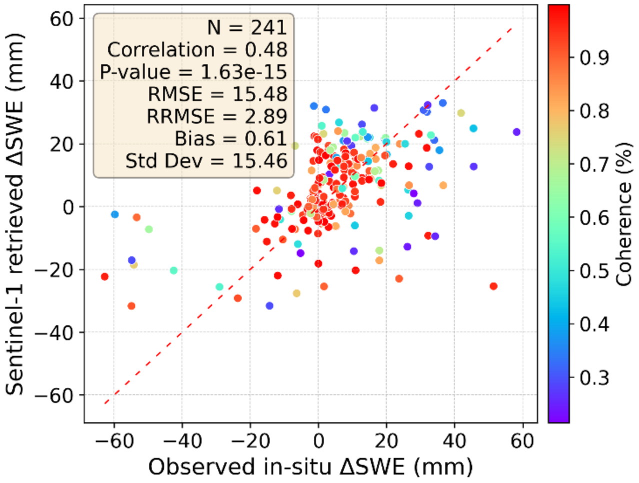

Figure 10: Comparison between the in-situ SWE changes in 12 days and the Sentinel-1 InSAR retrieved SWE changes at Altay in 2019-2021. (The color of the points corresponds to the coherence.)

As illustrated in the previous section, there are some differences in spatiotemporal cumulative SWE in the two snow seasons. To examine whether the differences in spatiotemporal cumulative SWE between the two seasons introduce errors or affect retrieval accuracy, the total validation results are divided by year, with each time series InSAR pair assessed separately (see Fig. 11). The validation results remain still reliable, with slightly better performance when analyzed separately for each snow season rather than combined. This indicates the stability of the retrieval method across different snow seasons.

The retrieved ΔSWE are validated against in-situ ΔSWE with an RMSE of 15.92 mm (R=0.47, p-value<<0.5) in 2019-2020,14.79 mm (R=0.51, p-value<<0.5) in 2020-2021. The points that belong to higher coherence (circled) InSAR pair are closer to the 1:1 line, showing a good agreement in the retrieved and in-situ ΔSWE. While it turns to wet snow, retrieved ΔSWE has a shorter dynamic change range than in-situ ΔSWE values. This is demonstrated by the red points (from March to April), which have a total dynamic range of around 120 mm of in-situ ΔSWE but 20 mm in retrieved SWE in Fig. 11 (a), and have a total dynamic range of around 100 mm in in-situ ΔSWE but 40mm in retrieved ΔSWE in Fig. 11 (b). This may be due to the uncertainty of the observed and retrieved SWE during the melting process of snow, suggesting the retrieval range is saturated.

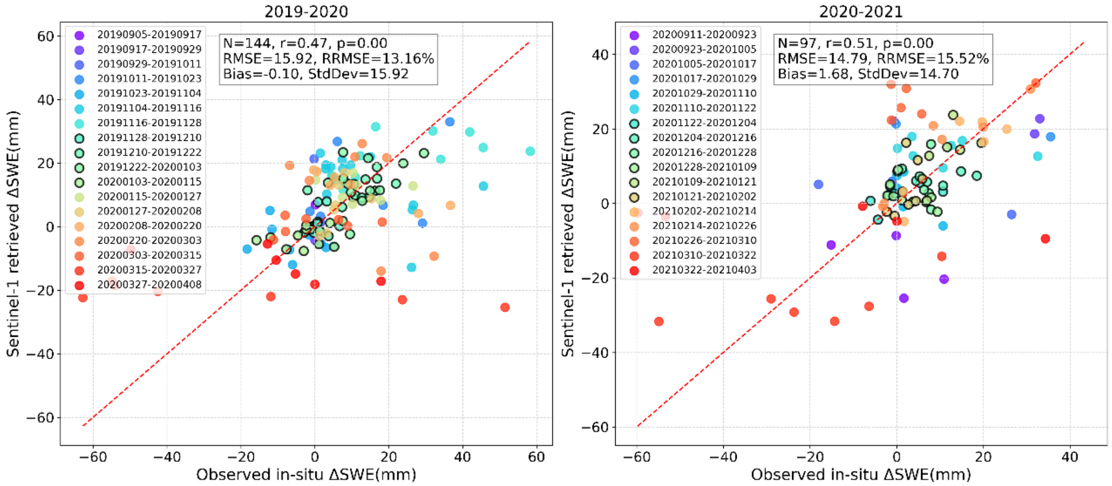

Figure 11: Comparison between the in-situ SWE changes in 12 days and the Sentinel-1 InSAR retrieved SWE changes at Altay in the snow seasons of (a) 2019-2020 and (b) 2020-2021. (The color of the points corresponds to each InSAR pair. The points with higher coherence in the whole InSAR pair scene are circled.)

4.3.2 Validation results under different numbers of selected points

The calibration in the InSAR-derived SWE is necessary because it's hard to find a stable point at the ground owing to the whole scene being covered by snow. Each InSAR pair needs to be calibrated. The calibration parameters can be chosen using all or part of the in-situ SWE observations. Various strategies of point selection may generate varied validation results. Due to the limited observations (some InSAR pairs only have one in-situ SWE observation; see Fig. 12), we do not choose calibration points based on properties (e.g., elevation, air temperature, snow density). Therefore, the strategy is conducted based on the Monte Carlo (100 times) randomly selected number of points for calibration.

Based on the method introduced in Section 3.4.2, part of the SWE observations in each InSAR pair in 2019-2020 are used to derive the calibration parameter. Then, the rest of the SWE observations are used to validate the retrieved SWE after calibrating each InSAR pair using the derived calibration parameter. As shown in Fig. 12, the maximum number of available SWE observations in all InSAR pairs in 2019-2020 snow season is 13. Hence, the maximum number of points used for calibration is limited to 10 to ensure that at least 3 points remain for validation. One hundred tests based on the random point selection method with different numbers of points are carried out, and the following validation results are shown in Figs. 13 and 14.

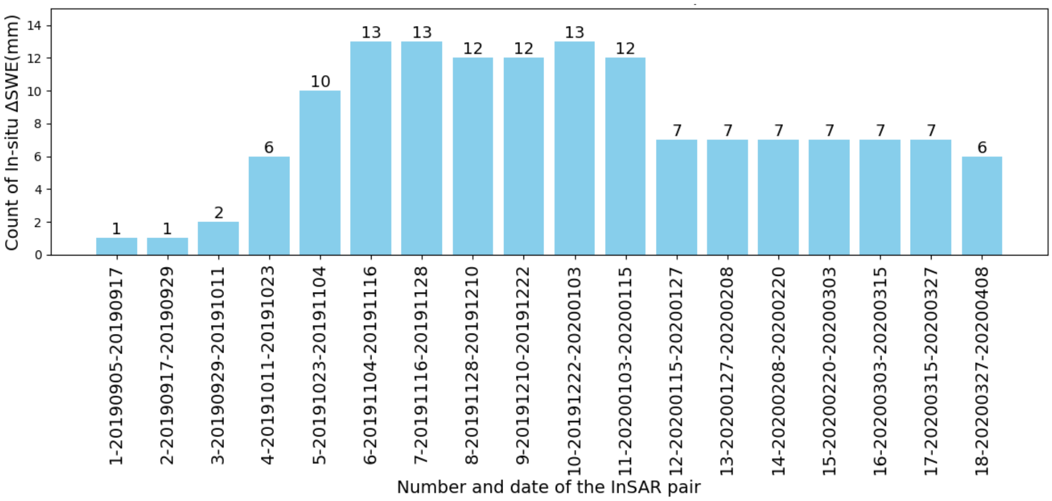

440 **Figure 12: The number of in-situ ΔSWE in each InSAR pair in 2019-2020**

Validation results under different numbers of selected calibration points after 100 Monte Carlo random tests are presented in Fig. 13. The validation shows that accuracy changes as the number of points changes. In particular, accuracy arises as the number of calibration points increases from 1 to 5 at first, then stabilizes when the number of calibration points varies between 5 and 7. However, as the number of calibration points increases beyond 7, the rapid reduction in validation points is likely the main reason for a bad validation result.

This trend is further illustrated in a scatter plot comparing the in-situ SWE changes with the Sentinel-1 InSAR-derived SWE changes for one representative realization out of the 100 trials under different numbers of selected calibration points (from 1 to 10), see Fig. 14. The results show good validation performance when using 5, 6, or 7 calibration points. This finding suggests that selecting at least half of the available SWE values for calibration can yield reliable InSAR-derived SWE estimates.

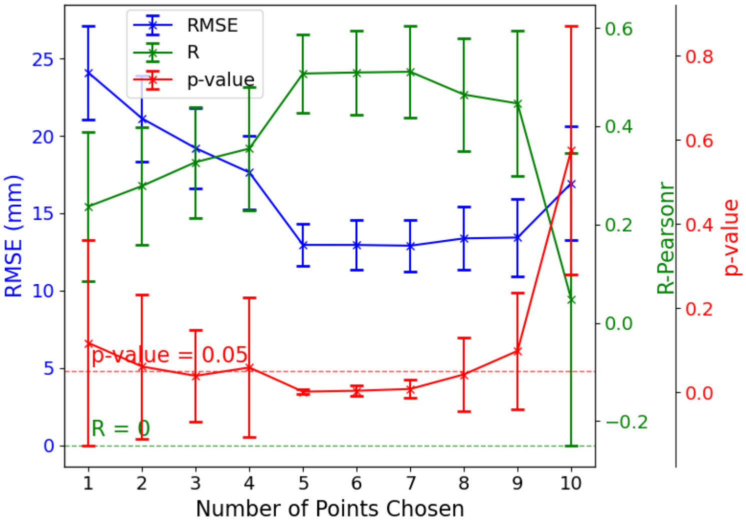

Figure 13: Variation of RMSE, Pearson correlation, and p-value with the number of points used for calibration after 100 Monte Carlo random point selection tests. (The two ends of the long line represent the range, and the '×' symbol in the middle represents the average value over 100 times.) 455

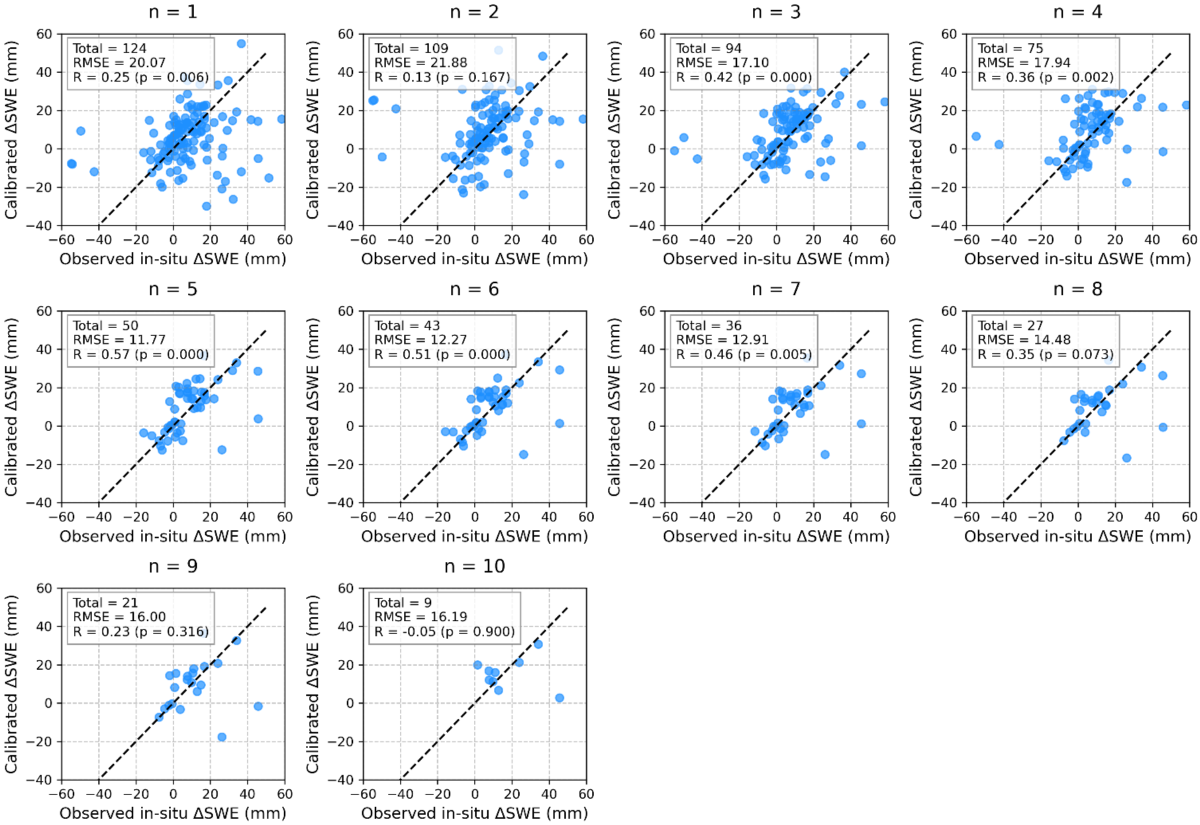

Figure 14: Comparison between the in-situ SWE changes and the Sentinel-1 InSAR retrieved SWE change under different numbers of selected calibration points, from 1 to 10, in one realization.

4.4 Comparing Sentinel-1 retrieved cumulative SWE with in-situ cumulative SWE

All of the time series retrieved ΔSWE are used to calculate the retrieved cumulative SWE at each date from the start date of our satellite's observation date, which can be expressed as

$$SWE(t_{i+1}) = SWE(t_0) + \sum_{t_j=t_0}^{t_i} \Delta\mathrm{SWE}(t_j, t_{j+1}) \tag{22}$$

where t_0 is the start date (September 5, 2019 or September 11, 2020), $SWE(t_{i+1})$ is the cumulative (or absolute) SWE on the date of t_{i+1}, and $\Delta\mathrm{SWE}(t_j, t_{j+1}) = \mathrm{SWE}(t_{j+1}) - \mathrm{SWE}(t_j)$. For example, the cumulative SWE at 20190929 (yyyymmdd) is the summation of the cumulative SWE at the initial date of 20190905, $\Delta\mathrm{SWE}(20190905{,}20190917)$, and $\Delta\mathrm{SWE}(20190917{,}20190929)$.

It should be noted that discrepancies in initial SWE values may exist when comparing cumulative SWE from in-situ measurements and that derived from InSAR observations. To ensure a consistent basis for comparison, an initial value alignment is performed before the validation analysis. On the one hand, the satellite-derived SWE is referenced to the first Sentinel-1 acquisition, where the initial SWE is set to zero. However, at the same time, a few in-situ stations may record small but nonzero SWE values due to early snowfall events. On the other hand, for most stations, no snowfall is recorded on the date of the first acquisition or even several subsequent acquisitions, so the measured cumulative SWE remains zero. In contrast, the InSAR-derived cumulative SWE may show nonzero values at the same acquisition due to atmospheric effects or other factors accumulating over time. As a result, inconsistencies in initial SWE values may also occur at later dates, even when no snowfall is observed. This discrepancy introduces a constant offset when comparing the retrieved cumulative SWE with in-situ data. To eliminate this offset and ensure consistency in the initial comparison, the satellite-derived cumulative SWE is adjusted to match the first available in-situ cumulative SWE observation on the same date. This alignment procedure is then applied to all subsequent satellite-derived cumulative SWE values.

4.4.1 Validation of retrieved cumulative SWE

As shown in Fig. 15, the retrieved cumulative SWE is validated against in situ SWE observations after excluding wet snow conditions, with an RMSE of 36.5 mm (R=0.63, p-value≪0.05). After this exclusion, some underestimated and scattered points deviate significantly from the 1:1 line. Most of these points correspond to high-elevation stations such as Wuxilike, Wuxilike-Muban, and Tollheit. The locations and elevations of these stations can be found in Fig. 2, and the cumulative SWE underestimation is illustrated later in Fig. 17 and Fig. 18. Tollheit is not shown due to the limited number of valid data points. Improved validation results are obtained by excluding these underestimated points, with an RMSE of 28.4 mm and R=0.78.

Heavy snowfall (around 100 mm) at the Wuxilike station (and nearby Wuxilike-Muban) in early Nov 2019 lead to low coherence and phase unwrapping errors (as in Fig. 5 and Fig. 7). This leads to ΔSWE underestimation errors propagating through the time series, so these stations are excluded from further validation.

The bimodal scatter distribution observed in the validation results is mainly attributed to the error propagation in the time series retrieved ΔSWE. Since cumulative SWE is calculated by summing ΔSWE from each interferometric pair, any overestimation or underestimation of ΔSWE in a single pair propagates through the subsequent cumulative SWE, leading to deviations (to be illustrated in detail in Fig. 21 and Fig. 22). As a result, the scatter tends to split around the 1:1 line, forming a bimodal pattern. Nevertheless, despite this apparent bimodal scatter distribution. In general, the higher in situ SWE values generally correspond to higher retrieved SWE values, which means the overall trend of the retrieved cumulative SWE remains consistent with the in-situ measurements.

Here, the wet snow points (light grey) are excluded. These points correspond to the end of the snow season (early March and later), when air temperature is above 0 °C, but the snowpack has not completely melted. Therefore, data from March 3, 2020, and from March 10, 2021 are removed, according to the SWE and air temperature time series shown in Fig. 7. This exclusion is primarily due to the limited penetration depth of C-band radar signals in wet snow, which restricts the ability to retrieve reliable SWE estimations under such conditions. To better understand this limitation, the physical basis of wet snow interaction with radar signals is briefly discussed below.

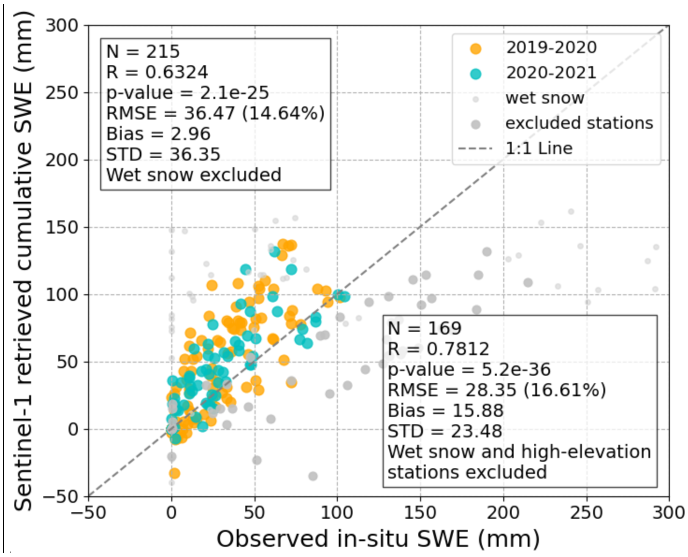

Figure 15: Comparison between the Observed in-situ SWE and the Sentinel-1 InSAR retrieved cumulative SWE at Altay in 2019-2021.

The penetration depth of a medium δ_p is related to the volume absorption coefficient κ_a as

$$\delta_p = \frac{1}{\kappa_a} \tag{23}$$

κ_a is related to the effective dielectric constant of the wet snow ε_{ws} as

$$\kappa_a = \frac{4\pi}{\lambda} Im\{\sqrt{\varepsilon_{ws}}\} \tag{24}$$

The permittivity of wet snow at C-band (5.405GHz) can be given by the following equations from the modified Debye-like model (Hallikainen et al., 1986):

$$\varepsilon_{ws} = \varepsilon_{ws}' - j\varepsilon_{ws}'' \tag{25}$$

$$\varepsilon_{ws}' = 1 + 1.83\rho_s + 0.02m_v^{1.015} + 0.0539m_v^{1.31} \tag{26}$$

$$\varepsilon_{ws}'' = 0.0321m_v^{1.31}$$

where ρ_s is the snow density (g/cm^3), and m_v is the volume fraction of liquid water in the snow mixture (%).

As shown in Fig. 16 (A), significant differences exist in the interaction mechanisms between electromagnetic waves and dry snow versus wet snow. Electromagnetic waves interact primarily with the surface layer of wet snow, resulting in an increase of the scattering phase center compared to dry snow. This leads to a loss of coherence between the wet snow signal and the previous snow-free observation. Particularly at the end of the snow season, the C-band electromagnetic waves can not penetrate the snow to the ground with the increase of m_v caused by the snow melt process. For example, in Fig. 16 (B), a penetration depth δ_p of approximately 5 cm is observed when m_v is 6%, but usually the snow depth is larger than 20 cm. Under these conditions, errors will be introduced if the retrieval algorithm (3) for dry snow scenarios is applied. Therefore, the wet snow data are excluded during the validation.

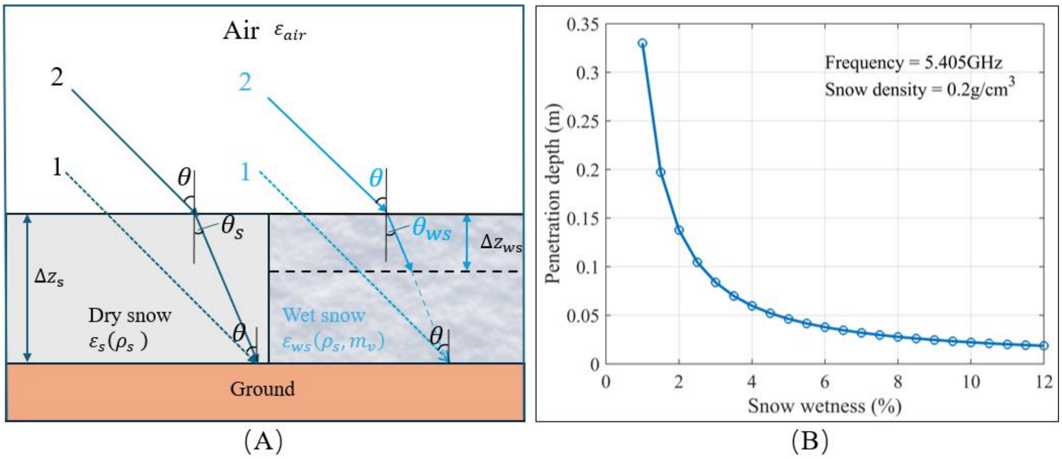

Figure 16: (A) Propagation path of radar wave in dry snow and wet snow, and (B) penetration depth of wet snow at the frequency of 5.405 GHz and the snow density of 0.2 g/cm^3.

https://doi.org/10.5194/egusphere-2025-2329
Preprint. Discussion started: 11 June 2025

4.4.2 Comparing Sentinel-1 retrieved time series cumulative SWE with in-situ cumulative SWE

The time series of retrieved cumulative SWE is evaluated at each in-situ SWE station (Figs. 17 and 18, for each year, respectively). Good agreements are shown between the in-situ and retrieved cumulative SWE at some stations, such as stations (6), (8), and (14) in Fig. 17 and station (15) in Fig. 18. Nevertheless, an overestimation of about 20 to 80 mm is exhibited by the satellite retrieval at some stations (i.e., the blue in-situ SWE line is lower) in two snow seasons (stations (13) and (17)). In contrast, station (12) is underestimated by about 80 mm in mid-December (i.e., the blue in-situ SWE line is higher) in two snow seasons. These overestimation and underestimation for two consecutive years may be related to the inherent environment of each site. For example, underestimation occurs at station (12), located in relatively higher elevations (around 2146 m), while overestimation is observed at stations (13) and (17), situated in lower elevations (around 1076 m and 730 m, respectively). These differences may be attributed to variations in local slope, surface conditions, and nearby mountainous areas, which together affect the interferometric phase signal and introduce biases in the retrieved SWE. At the Wuxilike station (Fig. 17(9)), heavy snowfall is recorded from early November to early December. Although an increasing trend is captured in the retrieval, a notable underestimation remains, owing to decorrelation and phase unwrapping errors caused by heavy snowfall. This tim-series result is consistent with the above temporal decorrelation analysis (Fig. 5 and Fig. 7) as well as the underestimation of the cumulative SWE in Fig. 15.

However, some sites show different estimations (overestimation in one year and underestimation in another year) in two years. This phenomenon may be related to the different snow cumulations over the two years. Another reason might be that the errors will accumulate as time passes. This means one pair of overestimations and underestimations will propagate on the following cumulation estimations. Moreover, the overestimated station may become underestimated after the phase calibration process, or vice versa. The choice of pixel averaging can affect the final retrieval results, too. For example, at station (14) Xiaodonggou in Fig. 17, the retrieval accuracy improves as the averaging window size increases. This may be related to the mountainous terrain rather than the uniform plain surrounding the station, where a larger averaging window may have more impact on the retrieval results. Despite some overestimation and underestimation, the retrieved SWE trends are generally consistent with in-situ measurements across all stations, which agrees with the findings of Shadi et al. (2023), who suggest that the main reason for these discrepancies is likely related to phase unwrapping errors and phase ambiguities.

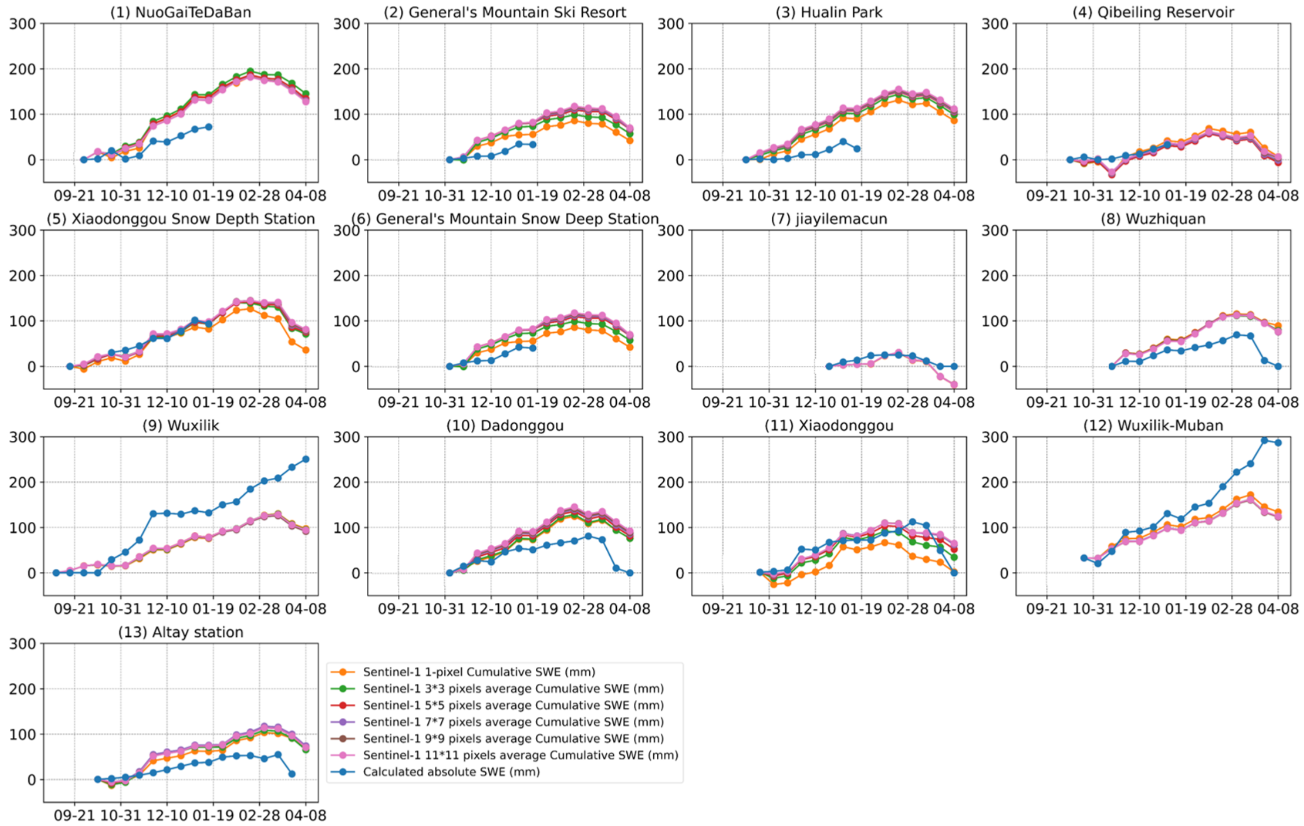

550 **Figure 17: Time series of in-situ and retrieved cumulative SWE using Sentinel-1 interferometric phase for different stations in Altay during the 2019-2020 snow season. (The in-situ cumulative SWE is represented by blue lines, while the retrieved cumulative SWE is shown by six different colored lines, each corresponding to a different spatial scale. Specifically, the retrieved SWE values are calculated as the average SWE within a window centered at the station's latitude and longitude, with window sizes of 1×1, 3×3, 5×5,**
555 **7×7, 9×9, and 11×11 pixels, respectively. The number in the upper right corner is the elevation of the site. The same color scheme apply to the following Fig. 18 for the 2020–2021 snow season.)**

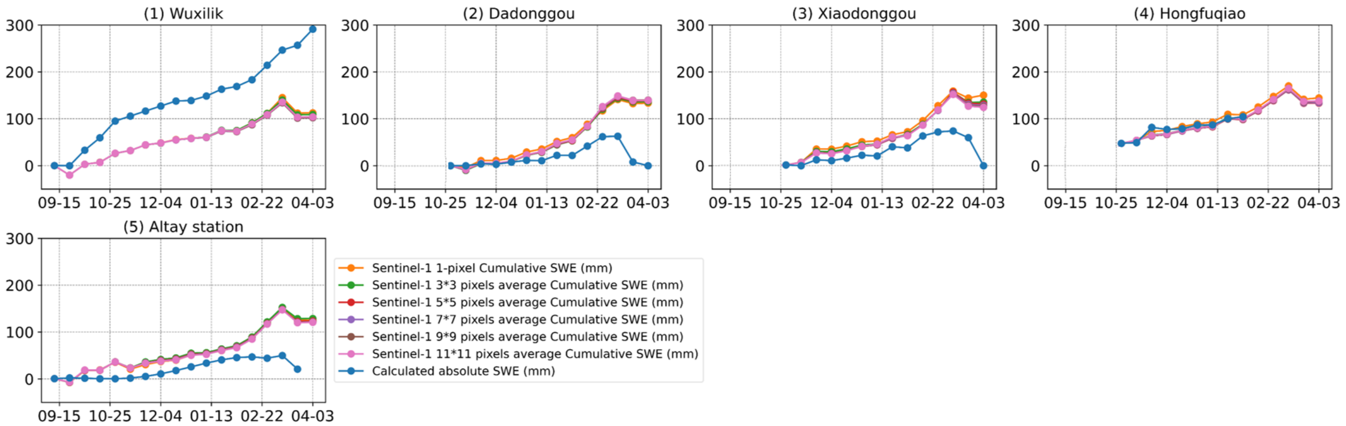

Figure 18: Time series of in-situ and retrieved cumulative SWE using Sentinel-1 interferometric phase for different stations in Altay
560 **during the 2020-2021 snow season.**

https://doi.org/10.5194/egusphere-2025-2329
Preprint. Discussion started: 11 June 2025

5 Discussion

Good inversion performance is demonstrated in Section 4 in general, but some inconsistencies between retrieved and measured SWE can be seen, which are yet to be further investigated. For example, the abnormal points in the left area of Fig. 10, which are far from the 1:1 line, and the overestimation and underestimation of retrieved cumulative SWE in Figs. 15 and 16. In this section, we explore why different points show varied accuracy and what the optimal occasions of this retrieved method are by using available data on meteorology and snow properties. Then, the validation of cumulative SWE and ΔSWE at the same site is shown next with the scatterplot. At the end of this section, the effects of partial phase calibration on the inversion result are studied.

5.1 Analysis of multiple factors influencing the retrieval of ΔSWE

This section investigates the influence of various factors, including coherence, air temperature, elevation, slope, snow depth, and snow density, on the validation of retrieved ΔSWE, as illustrated in Fig. 19. Abnormal points, marked by rectangular frames in Fig. 19 (1), represent values where the in-situ ΔSWE is less than -40 mm while the retrieved ΔSWE exceeds -40 mm. As seen in Fig. 11 of Section 4.3.1, these points predominantly occur in the snowmelt season from March to April. During this period, the snow depth is primarily less than 20 cm, and snow density values in Fig. 19 (6) are relatively high (red and orange points greater than 200 kg/m³). This is consistent with the shallow snow and high density observed in ERA5 during the snowmelt season.

For points outside the abnormal area, those with lower coherence (purple) become more scattered, as shown in Fig. 19 (1). As shown in Fig. 19 (2), the lowest temperature (purple) values cluster around the 1:1 line. Except for the rectangular frames, points at lower elevations (Fig. 19 (3)) appear more accurate, and red points at high altitudes tend to show an underestimation. When both ΔSWE inversion and in-situ measurements are positive, snow density remains relatively constant (around 160 kg/m³). However, when ΔSWE is negative, snow densities are more varied due to snow melting, showing both lower values (purple points at 120 kg/m³) and higher values (red points at 200 kg/m³).

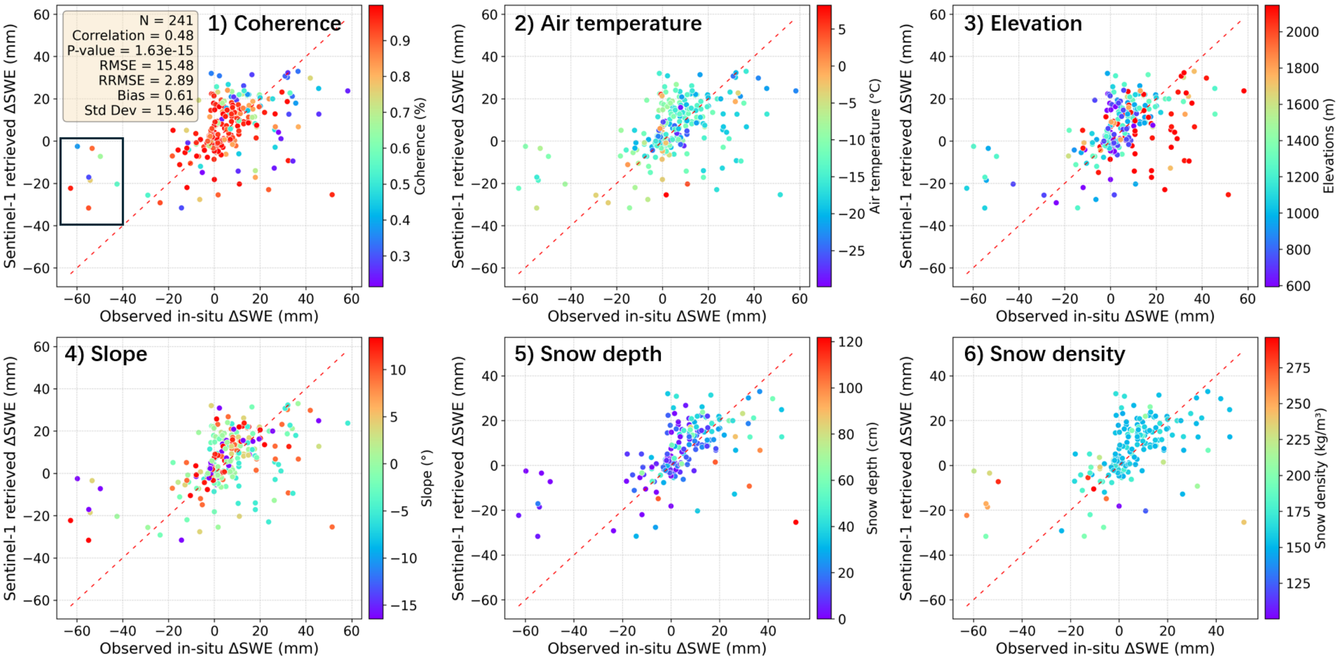

Figure 19: Analysis of multiple factors influencing the retrieval of ΔSWE. (Each sub-figure is colored based on different properties)

Additionally, data is removed based on specific thresholds for each factor to assess the impact on inversion results, as summarized in Table 1. For coherence, the threshold for removing low values was gradually increased from 0.3 to 0.6 (with no points having coherence below 0.2). After removing low-coherence points, inversion results show minimal changes, with a slight decrease in RMSE and correlation. This may be because only 22% of points have coherence below 0.6, and more than half (53%) have coherence above 0.9. When filtering higher temperature values (from 0 °C to -20 °C, decreasing by 5 °C), significant improvements are observed after removing points above -20 °C. The correlation increased to 0.77, and RMSE decreased to 9.8 mm. These points, corresponding to temperatures below -20 °C, are from four InSAR pairs collected from November to January during the dry snow season. For elevation and slope, the inversion results after limiting these ranges may not be entirely reliable, as the data distribution is not balanced (see histograms in Fig. 19 (c) and (d)), and the total number of data points is relatively small. Elevation and slope are intrinsic to the site, meaning each station corresponds to specific values of elevation and slope. Regarding snow depth, we test removing points with thick and shallow snow depths, retaining points with snow depths in a certain range, and removing thick snow (from 20 cm to 140 cm, increasing by 20 cm). The best results are obtained by retaining only points with snow depths between 0 cm and 20 cm, where the R-value reached 0.72 and RMSE was 12.1 mm. This could be attributed to the larger proportion of shallow snow (below 20 cm) in the dataset (38%, as shown in Fig. 19), compared to other depth ranges. For snow density, limiting the snow density in the scatter plot to between 150 kg/m^3 and 200 kg/m^3 will improve the results with an RMSE of 0.56 and RMSE of 12.24 mm.

Table 1: The validation results based on filtering of different parameters

1) coherence(%)

filter out range	RMSE(mm)	R	Total number
<0.3	15.23	0.44	230
<0.4	14.86	0.41	217
<0.5	14.86	0.40	205
<0.6	14.97	0.35	195

2) Air temperature(℃)

filter out range	RMSE(mm)	R	Total number
≥0	15.45	0.49	236
≥-5	15.7	0.47	218
≥-10	15.42	0.41	197
≥-15	15.33	0.40	105
≥-20	**9.54**	**0.77**	**33**

3) Elevations(m)

filter out range	RMSE(mm)	R	Total number
≥2000	**14.43**	**0.56**	**199**
≥1500	14.69	0.54	177
≥1000	14.55	0.37	105
≥600	11.93	0.46	26

4) Slope(°)

filter out range	RMSE(mm)	R	Total number
≥0	16.59	0.44	99
≤0	15.85	0.45	150
remain range			
-5<slope<5	14.74	0.43	121
-3<slope<3	**11.78**	**0.54**	**90**
-1<slope<1	12.44	0.50	46

5) Snow depth(cm)

remain range	RMSE(mm)	R	Total number
10<SD<80	11.79	0.60	111
20<SD<80	12.34	0.56	74
20<SD<40	12.62	0.56	46
40<SD<60	12.64	0.55	23
0<SD<20	**12.06**	**0.72**	**75**
0<SD<40	12.28	0.65	121
0<SD<60	12.34	0.65	144
0<SD<80	12.2	0.66	149
0<SD<100	12.39	0.64	152
0<SD<120	12.81	0.62	155
0<SD<140	14.17	0.54	156

6) Snow density(kg/m3')

remain range	RMSE(mm)	R	Total number
150<density<200	12.24	0.56	156
180<density<200	15.55	0.65	22

Original validation

	RMSE(mm)	R	Total number
without filtering	16.15	0.44	248

In conclusion, better validation results can be obtained by filtering temperature to below -20 °C, snow depth to 0-20 cm, and snow density to 150-200 kg/m³ in this study. However, the coherence, elevation, and slope limits do not significantly improve the inversion results. These findings are likely influenced by the distribution of properties. To describe the effect of uneven data distribution, histograms for each attribute are plotted (Fig. 20). More than half of the coherence values are in the range above 0.9, 40% of snow depths are in the 0-20 cm range, snow density is concentrated between 150-160 kg/m³, and 68% of temperature values located between -20 °C and -10 °C. Elevation and slope angles are less continuous due to the limited station distribution. These characteristics may suggest that similar properties are required to achieve inversion results comparable to ours.

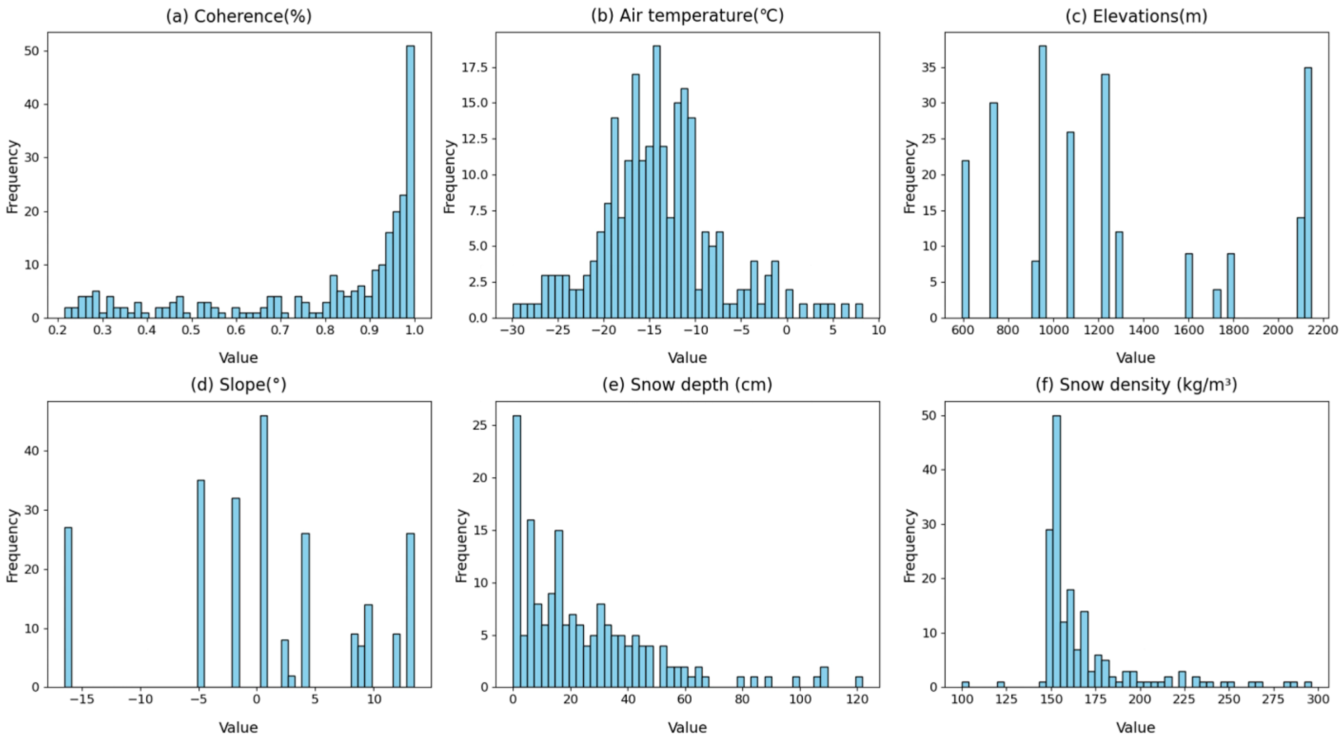

Figure 20: Histograms of various attributes of the validation point

5.2 Delta and cumulative in-situ SWE and retrieved SWE comparison at each station

Based on the distribution of in-situ and retrieved ΔSWE results validation at each station, the comparison data are classified into two groups. The classification in Fig. 21 shows a more concentrated distribution along the 1:1 line, while a more dispersed pattern is shown in Fig. 22.

The accuracy of cumulative SWE is directly influenced by the accuracy of ΔSWE, since cumulative SWE is calculated by accumulating ΔSWE values. For example, when ΔSWE is close to the 1:1 line, the cumulative correlation is also observed to be close to the 1:1 line (blue points in Figs. 21 (a) and (d), (c) and (f)). However, as cumulative SWE increases, it tends to scatter more from the 1:1 line, showing a consistent trend of overestimation or underestimation through error propagation based on the time series accumulation. In contrast, there are cases where the ΔSWE's validation does not show a good relationship, yet the cumulative SWE does, as shown in Figs. 22 (d) and (e). Similarly, with higher cumulative SWE values, data points increasingly deviate from the 1:1 line. Factors such as removing tropospheric error during processing may contribute to these discrepancies. Additionally, the reason may be variations in the station environment and errors in the in-situ data observations. The cumulative SWE is more prone to random error, which propagates to other pairs.

Furthermore, the scattered point distribution for different years at the same station exhibits similarities. This consistency suggests that patterns of overestimation and underestimation in delta and cumulative values may stem from the station's properties or observation biases.

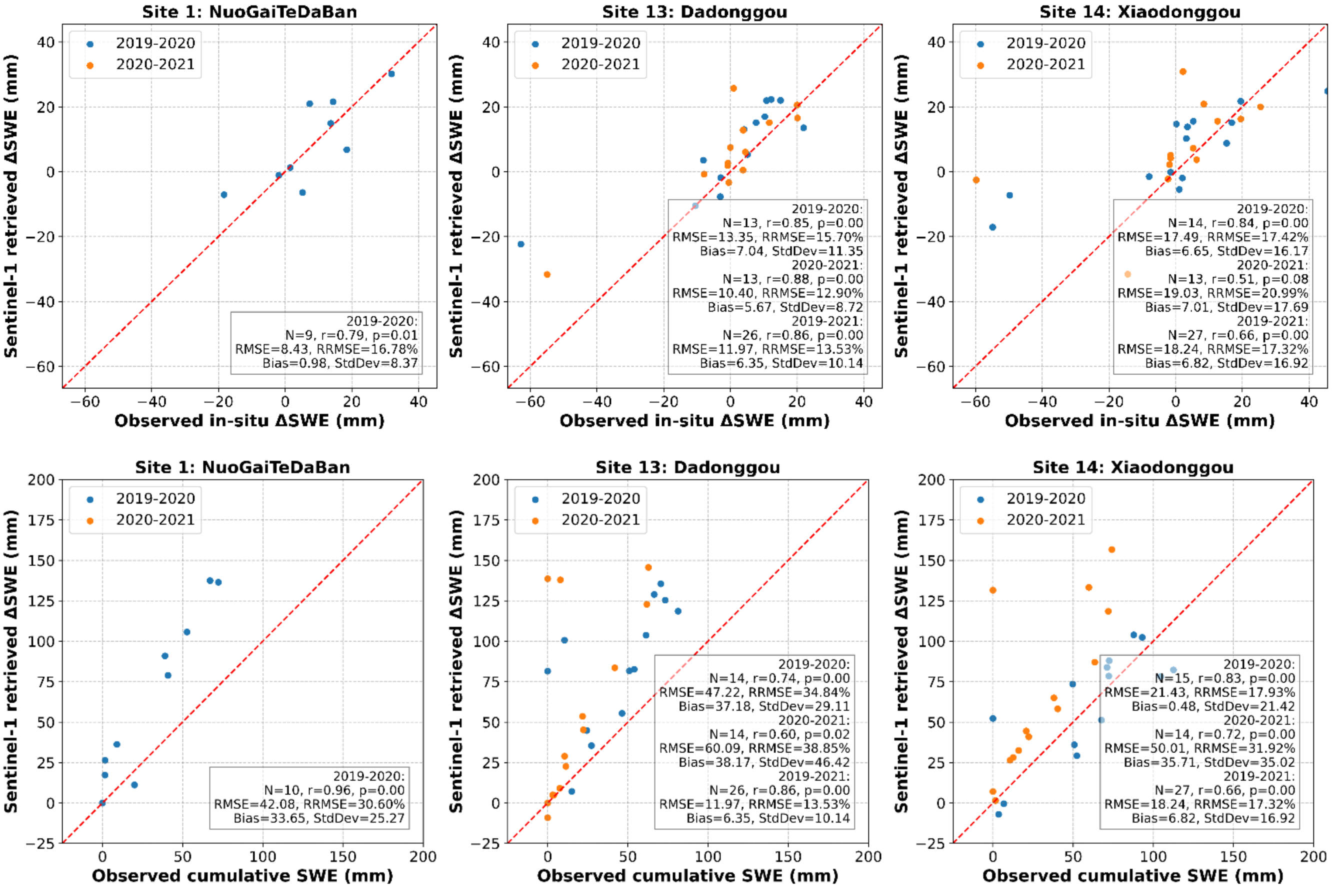

Figure 21: Comparison between the in-situ SWE changes and the Sentinel-1 InSAR retrieved SWE changes at three stations in Altay. (The top row is ΔSWE, and the bottom row is cumulative SWE; each column corresponds to the same station)

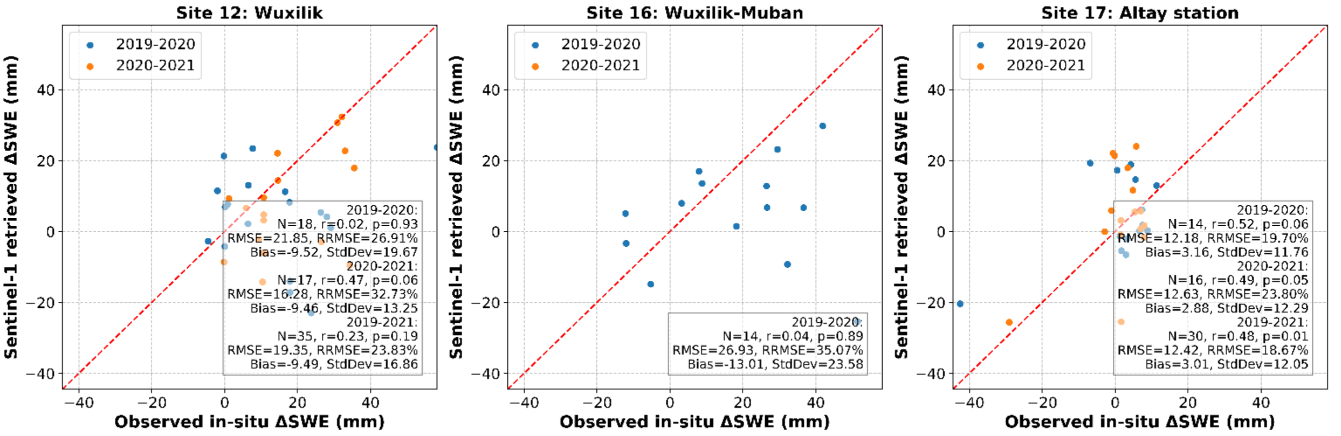

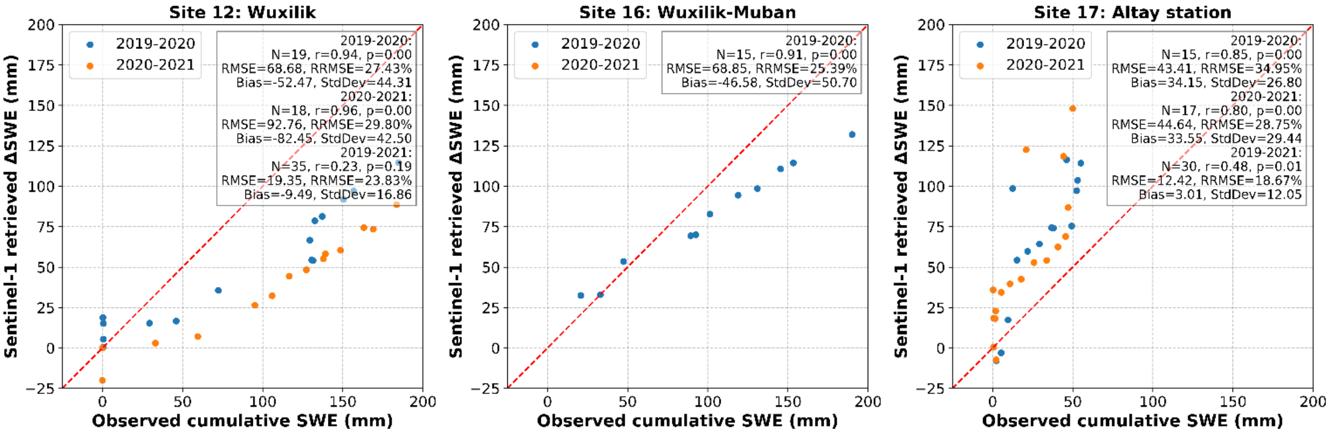

Figure 22: Comparison between the in-situ SWE changes and the Sentinel-1 InSAR retrieved SWE changes at the other three stations in Altay

5.3 The effects of partial phase calibration on validation of retrieved ΔSWE

Based on the method described in Section 3.4.3, the effects of partial calibration on the validation of retrieved ΔSWE are tested. The results are shown in Fig. 23. In case (A), where no calibration is used, the validation shows a poor agreement, with no significant correlation (R = 0.09). In case (B), applying only the integer multiple of 2π part, the validation improves substantially with an RMSE of 17.4 mm (R=0.36). In case (C), using the full calibration parameter, futher improvement is observed with an RMSE of 14.9 mm (R=0.52). Note that a total of 233 points are used in this validation, slightly fewer than the 241 in Fig. 10, due to the removal of a few outliers.

These results demonstrate that our phase calibration is essential for improving the accuracy of the InSAR-based ΔSWE retrieval. While the integer multiple of 2π accounts for the main portion of the phase error, the residual phase (that is caused by data processing errors, DEM residual error, atmospheric delays, systematic phase calibration error, and etc) still has a noticeable effect. Comparison to case (B) and (C) shows lower RMSE and bias, as well as an higher correlation, confirming the importance of calibrating the residual phase component. It can also be observed that the overall performance is improved through phase calibration, while some points with initially good agreement deviate from their previous alignment. In conclusion, the best accuracy can be achieved when the full calibration parameter is applied.

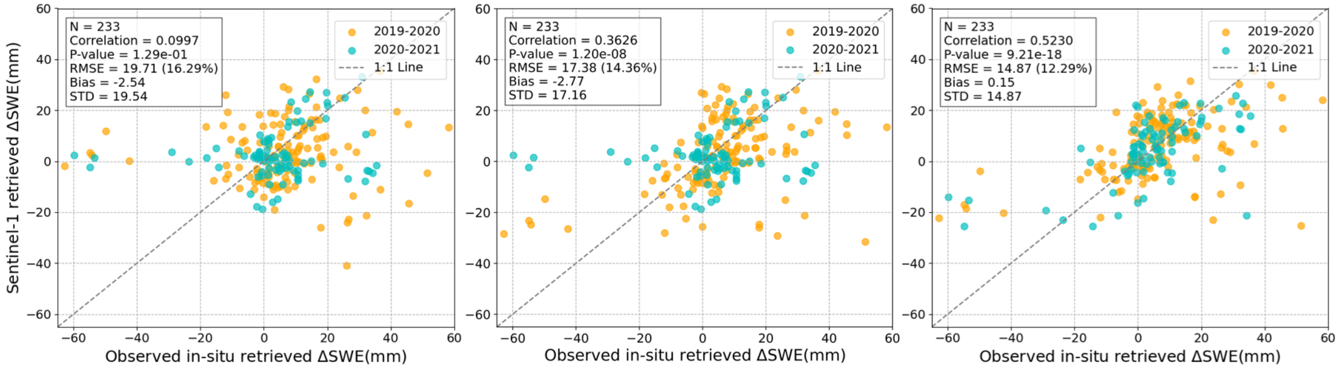

(A) Not use the calibration parameter (B) Use 2π part of the calibration parameter (C) Use the calibration parameter

Figure 23: Comparison of the validation results for in-situ ΔSWE changes in 12 days under different calibration strategies: (A) no calibration, (B) calibration using only the integer multiple of 2π part, and (C) using the full calibration parameter.

6 Conclusions

In this paper, Sentinel-1 time series data collected every 12 days from 2019 to 2021 are used to retrieve changes in SWE (ΔSWE) and cumulative SWE throughout the entire snow season. A specific frame is selected to include 15 in-situ stations over Altay. An adequate correlation (R=0.48) is observed between the retrieved 12-day ΔSWE and the in-situ values, with an RMSE of 15 mm over two years. The RMSE slightly improves in the second year, showing values of 14.79 mm (R=0.51) for 2020-2021. It should be noted that inversion results are not filtered for low coherence or high temperatures above 0℃ across the full snow season. Considering that the nearly global consistent coverage offered by Sentinel-1's 12-day repeat-pass imagery, the SWE inversion using Sentinel-1 and the InSAR method presented in this study, along with the analysis of multiple factors (such as coherence and air temperature) impact on the accuracy of this retrieval technique, can be applied to other snow-covered regions.

After excluding wet snow points, the retrieved cumulative SWE shows reasonable performance, with an RMSE of 36.5 mm (R=0.63). Further improvement is achieved by excluding high-elevation stations affected by early-season heavy snowfall that cause phase unwrapping errors, reducing the RMSE to 28.4 mm and increasing R to 0.78. The observations and inversion of time series cumulative SWE show consistency at several stations, albeit some stations indicate overestimations or underestimations. The scene-wide coherence, unwrapped phase, and cumulative SWE are displayed in the snow season from 2019-2021. The similarities of snow changes in two years can be found in these displays.

Moreover, a novel phase calibration method is introduced and validated by varying the total number of in-situ ΔSWE data for calibration. The results show that selecting at least half of the available ΔSWE values for calibration can yield reliable InSAR-derived ΔSWE estimates. Additionally, although applying only the integer multiple of 2π improves the results, better accuracy is achieved when the full calibration parameter is used. This suggests that the residual phase component has a pronounced contribution to the overall error and should not be ignored. Besides the results mentioned above, the factors that affect the performance of this approach are discussed, such as coherence, air temperature, and snow density. Higher coherence, lower temperatures, and more accurate snow density measurements are essential for achieving effective inversion results.

Regarding potential limitations, on one hand, it is noted that for the InSAR method to invert SWE effectively, longer wavelengths and shorter revisit times (which improve coherence) are necessary, as well as longer time series observations for better atmospheric effect estimation. This study uses C-band data with a 12-day revisit period, which can be improved using lower frequency bands (L-band) and shorter revisit intervals. On the other hand, stations that directly measure SWE are preferred, as many stations require snow density data, introducing some uncertainty into observations. Visual interpretation errors in snow depth measurements through snow sticks may also happen, particularly in sloped locations, which could amplify uncertainties. Despite these limitations, our validation results are still reasonable, providing a valuable reference for the broader application of 12-day revisited Sentinel data in SWE inversion studies.

7 Acknowledgments

The authors would like to acknowledge the European Space Agency (ESA) for providing Sentinel-1 data and the Altay Meteorological Bureau for supplying ground-based observational data used in this study. ChatGPT was used to enhance the clarity of some sentences. All revisions were carefully reviewed and revised by the authors. This work was financially supported by the Ministry of Science and Technology through the National Key R&D Program of China under grant number 2022YFB3903300 and grant number 2022YFB3903301.

References

Aguirre, F., Carrasco, J., Sauter, T., Schneider, C., Gaete, K., Garín, E., Adaros, R., Butorovic, N., Jaña, R., and Casassa, G.: Snow cover change as a climate indicator in Brunswick Peninsula, Patagonia, Frontiers in Earth Science, 6, 130, 2018.

Barnett, T. P., Adam, J. C., and Lettenmaier, D. P.: Potential impacts of a warming climate on water availability in snow-dominated regions, Nature, 438, 303-309, 2005.

Bonnell, R., Elder, K., McGrath, D., Marshall, H.-P., Starr, B., Adebisi, N., Palomaki, R., and Hoppinen, Z.: L-band InSAR snow water equivalent retrieval uncertainty increases with forest cover fraction, Geophysical Research Letters, 51, e2024GL111708, 2024.

Brown, R., Tapsoba, D., and Derksen, C.: Evaluation of snow water equivalent datasets over the Saint-Maurice river basin region of southern Québec, Hydrological Processes, 32, 2748-2764, 2018.

Dagurov, P., Chimitdorzhiev, T., Dmitriev, A., and Dobrynin, S.: Estimation of snow water equivalent from L-band radar interferometry: simulation and experiment, International Journal of Remote Sensing, 41, 9328-9359, 2020.

Dai, L., Che, T., Zhang, Y., Ren, Z., Tan, J., Akynbekkyzy, M., Xiao, L., Zhou, S., Yan, Y., and Liu, Y.: Microwave radiometry experiment for snow in Altay, China: time series of in situ data for electromagnetic and physical features of snowpack, Earth System Science Data, 14, 3509-3530, 2022.

Dai LiYun, D. L., Che Tao, C. T., Wang Jian, W. J., and Zhang Pu, Z. P.: Snow depth and snow water equivalent estimation from AMSR-E data based on a priori snow characteristics in Xinjiang, China, 2012.

Deeb, E. J., Forster, R. R., and Kane, D. L.: Monitoring snowpack evolution using interferometric synthetic aperture radar on the North Slope of Alaska, USA, International journal of remote sensing, 32, 3985-4003, 2011.

Derksen, C., Toose, P., Rees, A., Wang, L., English, M., Walker, A., and Sturm, M.: Development of a tundra-specific snow water equivalent retrieval algorithm for satellite passive microwave data, Remote Sensing of Environment, 114, 1699-1709, 2010.

Fattahi, H., Agram, P., and Simons, M.: A network-based enhanced spectral diversity approach for TOPS time-series analysis, IEEE Transactions on Geoscience and Remote Sensing, 55, 777-786, 2016.

Foster, J., Chang, A., and Hall, D.: Comparison of snow mass estimates from a prototype passive microwave snow algorithm, a revised algorithm and a snow depth climatology, Remote sensing of environment, 62, 132-142, 1997.

Fu, Q., Li, B., Hou, Y., Bi, X., and Zhang, X.: Effects of land use and climate change on ecosystem services in Central Asia's arid regions: a case study in Altay Prefecture, China, Science of the Total Environment, 607, 633-646, 2017.

Guneriussen, T., Hogda, K. A., Johnsen, H., and Lauknes, I.: InSAR for estimation of changes in snow water equivalent of dry snow, IEEE Transactions on Geoscience and Remote Sensing, 39, 2101-2108, 2002.

Hallikainen, M., Ulaby, F., and Abdelrazik, M.: Dielectric properties of snow in the 3 to 37 GHz range, IEEE transactions on Antennas and Propagation, 34, 1329-1340, 1986.

Hoppinen, Z. M., Oveisgharan, S., Marshall, H.-P., Mower, R., Elder, K., and Vuyovich, C.: Snow water equivalent retrieval over Idaho, Part B: Using L-band UAVSAR repeat-pass interferometry, The Cryosphere Discussions, 2023, 1-24, 2023.

Kellndorfer, J., Cartus, O., Lavalle, M., Magnard, C., Milillo, P., Oveisgharan, S., Osmanoglu, B., Rosen, P. A., and Wegmüller, U.: Global seasonal Sentinel-1 interferometric coherence and backscatter data set, Scientific Data, 9, 73, 2022.

King, J., Derksen, C., Toose, P., Langlois, A., Larsen, C., Lemmetyinen, J., Marsh, P., Montpetit, B., Roy, A., and Rutter, N.: The influence of snow microstructure on dual-frequency radar measurements in a tundra environment, Remote Sensing of Environment, 215, 242-254, 2018.

Lei, Y., Shi, J., Liang, C., Werner, C., and Siqueira, P.: Snow water equivalent retrieval using spaceborne repeat-pass L-band SAR interferometry over sparse vegetation covered regions, IGARSS 2023-2023 IEEE International Geoscience and Remote Sensing Symposium, 852-855,

Lei, Y., Zhou, J., Pan, J., Xiong, C., Xu, G., Shi, J., Wang, Z., and Fu, A.: Altay 2024: Synergetic Spaceborne Airborne Field Snow Campaign, IGARSS 2024-2024 IEEE International Geoscience and Remote Sensing Symposium, 1661-1664,

Leinss, S., Wiesmann, A., Lemmetyinen, J., and Hajnsek, I.: Snow water equivalent of dry snow measured by differential interferometry, IEEE Journal of Selected Topics in Applied Earth Observations and Remote Sensing, 8, 3773-3790, 2015.

Matzler, C.: Microwave permittivity of dry snow, IEEE Transactions on Geoscience and Remote Sensing, 34, 573-581, 1996.

Nagler, T., Rott, H., Scheiblauer, S., Libert, L., Mölg, N., Horn, R., Fischer, J., Keller, M., Moreira, A., and Kubanek, J.: Airborne experiment on InSAR snow mass retrieval in Alpine environment, IGARSS 2022-2022 IEEE International Geoscience and Remote Sensing Symposium, 4549-4552,

Oveisgharan, S., Zinke, R., Hoppinen, Z., and Marshall, H. P.: Snow water equivalent retrieval over Idaho–Part 1: Using Sentinel-1 repeat-pass interferometry, The Cryosphere, 18, 559-574, 2024.

Rott, H., Nagler, T., and Scheiber, R.: Snow mass retrieval by means of SAR interferometry, 3rd FRINGE Workshop, European Space Agency, Earth Observation, 1-6,

Rott, H., Yueh, S. H., Cline, D. W., Duguay, C., Essery, R., Haas, C., Hélière, F., Kern, M., Macelloni, G., and Malnes, E.: Cold regions hydrology high-resolution observatory for snow and cold land processes, Proceedings of the IEEE, 98, 752-765, 2010.

Rutter, N., Sandells, M. J., Derksen, C., King, J., Toose, P., Wake, L., Watts, T., Essery, R., Roy, A., and Royer, A.: Effect of snow microstructure variability on Ku-band radar snow water equivalent retrievals, The Cryosphere, 13, 3045-3059, 2019.

Shi, J. and Dozier, J.: Estimation of snow water equivalence using SIR-C/X-SAR, IGARSS'96. 1996 International Geoscience and Remote Sensing Symposium, 2002-2004,

Storvold, R., Malnes, E., Larsen, Y., Høgda, K., Hamran, S., Mueller, K., and Langley, K.: SAR remote sensing of snow parameters in norwegian areas—Current status and future perspective, Journal of Electromagnetic Waves and Applications, 20, 1751-1759, 2006.

Takala, M., Luojus, K., Pulliainen, J., Derksen, C., Lemmetyinen, J., Kärnä, J.-P., Koskinen, J., and Bojkov, B.: Estimating northern hemisphere snow water equivalent for climate research through assimilation of space-borne radiometer data and ground-based measurements, Remote Sensing of Environment, 115, 3517-3529, 2011.

Tedesco, M. and Jeyaratnam, J.: A new operational snow retrieval algorithm applied to historical AMSR-E brightness temperatures, Remote Sensing, 8, 1037, 2016.

Thakur, P. K., Aggarwal, S., Garg, P. K., Garg, R. D., Mani, S., Pandit, A., and Kumar, S.: Snow physical parameters estimation using space-based Synthetic Aperture Radar, Geocarto International, 27, 263-288, 2012.

Torres, R., Snoeij, P., Geudtner, D., Bibby, D., Davidson, M., Attema, E., Potin, P., Rommen, B., Floury, N., and Brown, M.: GMES Sentinel-1 mission, Remote sensing of environment, 120, 9-24, 2012.

You, Q., Wu, T., Shen, L., Pepin, N., Zhang, L., Jiang, Z., Wu, Z., Kang, S., and AghaKouchak, A.: Review of snow cover variation over the Tibetan Plateau and its influence on the broad climate system, Earth-Science Reviews, 201, 103043, 2020.

Yue, Z., Pengfeng, X., Xuezhi, F., Xueliang, Z., Yongke, Y., Lizao, Y., Chengxi, L., Guodong, B., and Rui, H.: Spatial distribution and features of the snow cover during accumulation period in the middle reaches of the Kelan River, Altay region, Xinjiang, Journal of Glaciology and Geocryology, 39, 979-988, 2017.

Yueh, S. H., Dinardo, S. J., Akgiray, A., West, R., Cline, D. W., and Elder, K.: Airborne Ku-band polarimetric radar remote sensing of terrestrial snow cover, IEEE Transactions on Geoscience and Remote Sensing, 47, 3347-3364, 2009.

Yueh, S. H., Xu, X., Shah, R., Kim, Y., Garrison, J. L., Komanduru, A., and Elder, K.: Remote sensing of snow water equivalent using coherent reflection from satellite signals of opportunity: Theoretical modeling, IEEE Journal of Selected Topics in Applied Earth Observations and Remote Sensing, 10, 5529-5540, 2017.

Yunjun, Z., Fattahi, H., and Amelung, F.: Small baseline InSAR time series analysis: Unwrapping error correction and noise reduction, Computers & Geosciences, 133, 104331, 2019.

Zhu, J., Tan, S., Tsang, L., Kang, D. H., and Kim, E.: Snow water equivalent retrieval using active and passive microwave observations, Water Resources Research, 57, e2020WR027563, 2021.